

The VIMOS VLT Deep Survey: Star formation rate density of Ly α emitters from a sample of 217 galaxies with spectroscopic redshifts $2 \leq z \leq 6.6^*$

P. Cassata¹, O. Le Fèvre², B. Garilli³, D. Maccagni³, V. Le Brun², M. Scodeggio³, L. Tresse², O. Ilbert², G. Zamorani⁴, O. Cucciati², T. Contini⁵, R. Bielby⁶, Y. Mellier⁶, H. J. McCracken⁶, A. Pollo⁷, A. Zanichelli⁸, S. Bardelli⁴, A. Cappi⁴, L. Pozzetti⁴, D. Vergani⁴, E. Zucca⁴

¹ Department of Astronomy, University of Massachusetts, Amherst, MA 01003, USA e-mail: paolo@astro.umass.edu

² Laboratoire d'Astrophysique de Marseille, UMR6110, CNRS-Université de Provence Aix-Marseille I, 38, rue Frédéric Joliot-Curie, F-13388 Marseille cedex 13, France

³ IASF-INAF - via Bassini 15, I-20133, Milano, Italy

⁴ INAF-Osservatorio Astronomico di Bologna - via Ranzani 1, I-40127, Bologna, Italy

⁵ Laboratoire d'Astrophysique de Toulouse-Tarbes, Université de Toulouse, CNRS, 14 Av. E. Belin, 31400 France

⁶ Institut d'Astrophysique de Paris, UMR7095 CNRS, Université Pierre et Marie Curie, 98 bis Boulevard Arago, 75014 Paris, France

⁷ The Andrzej Soltan Institute for Nuclear Studies, ul. Hoza 69, 00-681 Warszawa, Poland

⁸ IRA-INAF, Via Gobetti, 101, I-40129 Bologna, Italy

Received; accepted

ABSTRACT

Aims. The aim of this work is to study the contribution of the Ly α emitters to the star formation rate density (SFRD) of the Universe in the interval $2 < z < 6.6$.

Methods. We assembled a sample of 217 Ly α emitters (LAE) from the Vimos-VLT Deep Survey (VVDS) with secure spectroscopic redshifts in the redshift range $2 < z < 6.62$ and fluxes down to $F \sim 1.5 \times 10^{-18} \text{ erg/s/cm}^2$. 133 Ly α emitters are serendipitous identifications in the 22 arcmin² total slit area surveyed with the VVDS-Deep and the 3.3 arcmin² from the VVDS Ultra-Deep survey, and 84 are targeted identifications in the 0.62 deg² surveyed with the VVDS-DEEP and 0.16 deg² from the Ultra-Deep survey. Among the serendipitous targets we estimate that 90% of the emission lines are most probably Ly α , while the remaining 10% could be either [OII]3727 or Ly α . We computed the luminosity function and derived the star formation density from LAE at these redshifts.

Results. The VVDS-LAE sample reaches faint line fluxes $F(\text{Ly}\alpha) = 1.5 \times 10^{-18} \text{ erg/s/cm}^2$ (corresponding to $L(\text{Ly}\alpha) \sim 10^{41} \text{ erg/s}$ at $z \sim 3$) enabling the faint end slope of the luminosity function to be constrained to $\alpha \sim -1.6 \pm 0.12$ at redshift $z \sim 2.5$ and to $\alpha \sim -1.78_{-0.12}^{+0.10}$ at redshift ~ 4 , placing on firm statistical grounds trends found in previous LAE studies, and indicating that sub- L_* LAE ($L_{\text{Ly}\alpha} \lesssim 10^{42.5} \text{ erg/s}$) contribute significantly to the SFRD. The projected number density and volume density of faint LAE in $2 \leq z \leq 6.6$ with $F > 1.5 \times 10^{-18} \text{ erg/s/cm}^2$ are 33 galaxies/arcmin² and $\sim 4 \times 10^{-2} \text{ Mpc}^{-3}$, respectively. We find that the observed luminosity function of LAE does not evolve from $z=2$ to $z=6$. This implies that, after correction for the redshift-dependent IGM absorption, the intrinsic LF must have evolved significantly over 3 Gyr. The SFRD from LAE is found to be contributing about 20% of the SFRD at $z = 2 - 3$, while the LAE appear to be the dominant source of star formation producing ionizing photons in the early universe $z \sim 5 - 6$, becoming equivalent to that of Lyman Break galaxies.

Key words. Cosmology: observations – Galaxies: fundamental parameters – Galaxies: evolution – Galaxies: formation

1. Introduction

The Ly α line is the strongest hydrogen emission line in the Universe, and it is observed in the optical range for galaxies

at $z > 2$. It has thus naturally been used to search for high- z galaxies (Partridge&Peebles 1967; Djorgovski et al. 1985; Cowie & Hu 1998).

Send offprint requests to: P. Cassata

* Based on data obtained with the European Southern Observatory Very Large Telescope, Paranal, Chile, under Large Programs 070.A-9007 and 177.A-0837. Based on observations obtained with MegaPrime/MegaCam, a joint project of CFHT and CEA/DAPNIA, at the Canada-France-Hawaii Telescope (CFHT) which is operated by the National Research Council (NRC) of Canada, the Institut National des Sciences de l'Univers of the Centre National de la Recherche Scientifique (CNRS) of France, and the University of Hawaii. This work is based in part on data products produced at TERAPIX and the Canadian Astronomy Data Centre as part of the Canada-France-Hawaii Telescope Legacy Survey, a collaborative project of the NRC and CNRS.

The Ly α emission in galaxies is thought to be produced by star formation, as the AGN contribution to the Ly α population at $z < 4$ is found to be less than 5% (Gawiser et al. 2006; Ouchi et al. 2008; Nilsson et al. 2009). However, the physical interpretation of the observed Ly α flux is not simple, because the Ly α photons are resonantly scattered by neutral hydrogen. Ly α photons can therefore be more attenuated than other UV photons, and they have an escape fraction that can depend on the spatial distribution of neutral and ionized gas, as well as on the velocity field of the neutral gas (Giavalisco et al. 1996; Kunth et al. 1998; Mas-Hesse et al. 2003; Deharveng et al. 2008 and references therein).

Ly α emitters (LAE) observed up to now are forming stars at rates of $\sim 1 \div 10 M_{\odot} \text{yr}^{-1}$ (Cowie&Hu 1998; Gawiser et al. 2006; Pirzkal et al. 2007), and they have stellar masses as low as $10^8 \div 10^9 M_{\odot}$ and ages $< 50 \text{Myr}$ (Pirzkal et al. 2007; ; Gawiser et al. 2007; Nilsson et al. 2009). However, Nilsson et al. (2007) find ages between 0.1 and 0.9 Gyr, and more recently Pentericci et al. (2007) and Finkelstein et al. (2009) point out that Ly α galaxies are a more heterogeneous family than young star-forming galaxies: they also find Ly α emitters with old stellar populations (ages of $\sim 1 \text{Gyr}$) and a wide range of stellar masses (up to $10^{10} M_{\odot}$).

Interestingly, a class of Ly α galaxies with rest-frame equivalent width $EW > 240 \text{\AA}$ has been found (Malhotra&Roads 2002; Shimasaku et al. 2006). Galaxies with such large EW cannot be explained by star formation with a Salpeter IMF, but must have a top heavy IMF, a very young age $< 10^7 \text{yr}$ and/or a very low metallicity. Many of these large EW objects are spatially extended, and thus are good candidates to be cooling clouds or primeval galaxies (Yang et al. 2006; Schaerer 2002) and can give interesting clues about the first stages of star formation.

Together with studying the properties of Ly α galaxies at different redshifts, it is important to study the evolution of their luminosity function, comparing large and complete samples of Ly α galaxies at different redshifts. The most common technique used so far has been to build large samples from imaging in narrow band filters tuned to detect Ly α emission at $z \sim 2 \div 9$ (Hu et al. 2004; Cuby et al. 2003; Tapken et al. 2006; Kashikawa et al. 2006; Gronwall et al. 2007; Murayama et al. 2007; Ouchi et al. 2008; Nilsson et al. 2009; Guaita et al. 2010). Blank field spectroscopy has been used blindly to search for Ly α emitters in deep HST-ACS slitless spectroscopic observations (Malhotra et al., 2005) or slit spectroscopy (van Breukelen, Jarvis & Venemans 2005; Martin et al. 2008; Rauch et al. 2008; Sawicki et al. 2008), with Rauch et al. (2008) exploring the faintest emitters.

The general consensus today is that the apparent luminosity function of Ly α galaxies, that is the non-IGM corrected luminosity function, does not evolve at $z \sim 3 \div 6$ (Rhoads&Malhotra 2001; Ouchi et al. 2003; van Breukelen, Jarvis & Venemans 2005; Shimasaku et al. 2006; Murayama et al. 2007; Gronwall et al. 2007; Ouchi et al. 2008; Grove et al. 2009). However, this conclusion is drawn from small samples, as the narrow band imaging techniques sample only thin slices in redshift (typically $\Delta z=0.1$) and needs to be spectroscopically confirmed. Extensive spectroscopic follow-ups of narrow band Ly α candidates have been carried out in recent years, gathering hundreds of spectroscopic confirmations between $z \sim 2$ and $z \sim 7$. However, the spectroscopic coverage rarely reaches 30 \div 50% of the photometric sample (Murayama et al. 2007; Gronwall et al. 2007; Ouchi et al. 2008), but usually is much lower (Kashikawa et al. 2006; Nilsson et al. 2007; Matsuda et al. 2005). Moreover, current blind spectroscopic surveys sample only small areas to relatively shallow fluxes. It is likely that the apparent lack of evolution is a coincidence of the evolving intrinsic Ly α LF combined with an evolution of the intergalactic medium absorption with redshift (e.g. Ouchi et al. 2008). Firm conclusions about the possible evolution of the luminosity function have not yet been secured. Moreover, existing spectroscopic and narrow band samples are not sufficiently deep to constrain, even at intermediate redshift ($z \sim 3$), the slope of the luminosity function.

Measuring the luminosity function in turn enables to compute the luminosity density and star formation rate density evo-

lution under a set of well constrained hypotheses. The contribution of Ly α to the total star formation rate is yet not robustly measured mainly because the faint end slope of the luminosity function remains poorly constrained.

In this paper, we present the results from a very deep blind spectroscopic survey search of Ly α emitters over an unprecedented large sky area. We looked for the serendipitous detection of Ly α emission in the slits of the VIMOS VLT Deep Survey, concentrating on the VVDS-Deep and VVDS-Ultra-Deep surveys reaching up to 18h of integration on the VLT-VIMOS. We describe the spectroscopic and photometric data and the associated selection function in Section 2. The search for Ly α emitters and the final sample are presented in Section 3, and we discuss its properties in Section 4. The luminosity function calculation is discussed in Section 5, and the star formation rate density is derived. We discuss these results and give a summary in Section 6.

Throughout the paper, we use AB magnitudes and a standard Cosmology with $\Omega_M = 0.3$, $\Omega_{\Lambda} = 0.7$ and $h = 0.7$.

2. Search for serendipitous emission lines in the VVDS Deep and Ultra-Deep spectroscopic surveys

The Vimos-VLT Deep Survey (VVDS) exploited the high multiplex capabilities of the VIMOS instrument on the ESO-VLT (Le Fèvre et al., 2003) to collect more than 45000 spectra of galaxies between $z \sim 0$ and $z \sim 5$ (Le Fèvre et al., 2005; Garilli et al. 2008). In the VVDS-Deep 0216-04 field, more than ~ 10000 spectra have been collected for galaxies with $I_{AB} \leq 24$, observed with the LR-Red grism across the wavelength range $5500 < \lambda < 9350 \text{\AA}$, with integration times of 16000 seconds. In addition, the VVDS Ultra-Deep (Le Fèvre et al. 2010, in preparation) collected ~ 1200 spectra for galaxies with $i_{AB} \leq 24.75$, obtained with LR-blue and LR-red grisms, with integration times of 65000 seconds for each grism. This produces spectra with a wavelength range $3600 < \lambda < 9350 \text{\AA}$. For both the Deep and Ultra-Deep surveys, the slits have been designed to be 1" in width, providing a good sampling of the 1" typical seeing of Paranal, and between $\sim 4''$ and $\sim 15''$ in length, allowing good sky determination on both sides of the main target. The resulting spectral resolution is $R \simeq 230 - 250$ for both the LR-blue and LR-red grisms. The observations of the VVDS-Deep and Ultra-Deep have been taken in different observing runs split typically between 3 to 5 nights respectively. Given the Paranal seeing variations, the seeing quality of the final observations spans from 0.5" to 1.2" FWHM.

In this work, we take advantage of the fact that the VIMOS spectrograph produces a spectrum for the whole piece of sky covered by each slit. If a Ly α emitting galaxy with a redshift compatible with our wavelength range serendipitously falls in the slit, the Ly α line will appear in the 2-d spectrum. Obviously other line emitting galaxies at redshifts such that one or more of their emission line spectrum falls in the observed wavelength range will also be detected.

During the processing of the 2-d spectra of the VVDS main targets we identified that a population of serendipitous emission line objects was present. We therefore subsequently performed a systematic search for serendipitous emission line galaxies in the ~ 8000 Deep and ~ 1200 Ultra-Deep spectra. This was then followed by unambiguous redshift identification of all the line emitting galaxies as described in Section 3.2. A significant number of VVDS primary targets are also Ly α emitting galaxies (Le

Fèvre et al., 2010, in preparation), we added them to build a more complete LAE sample.

2.1. The dataset

The dataset consists of three sets of VIMOS pointings: the Deep, the Ultra-Deep blue, and the Ultra-Deep red. Each pointing consists of 4 separate quadrants, each containing approximately 100 slits. We summarize each dataset below:

- Deep dataset: it consists of 20 pointings, for a total of 80 quadrants and about 8000 slits; the main VVDS targets have been selected from an area of 0.62 deg^2 to have $17.5 \leq I_{AB} \leq 24$. The spectra have been obtained with the LR-Red grism, providing a wavelength range $5500 < \lambda < 9350 \text{ \AA}$. The exposure times are about 16000 seconds, allowing to reach fluxes as low as $\sim 5 \times 10^{-18} \text{ erg/cm}^2/\text{s}$ (see details below). The total sky area serendipitously covered is 22 arcmin^2 .
- Ultra-Deep dataset: it consists of 3 pointings, for a total of 12 quadrants and about 1200 slits; the main targets have been selected to have $23 \leq I_{AB} \leq 24.75$ from an area of 0.16 deg^2 . Each slit placed on a primary VVDS target has been observed twice, once with the LR-Blue grism, and once with the LR-Red. For the blue spectra, the spectral range is $3600 < \lambda < 6800 \text{ \AA}$, and for the red ones it is $5500 < \lambda < 9350 \text{ \AA}$. Thus, for each of the 1200 slits, the Ultra-Deep blue and red spectra overlap for about 1300 \AA . We did not try to combine spectra in the overlapping regions, because blue and red spectra have been observed under different sky background and atmospheric seeing conditions. As we will show in the next Sections, 13 Ly α emissions have been found in the overlapping regions. As we handled the blue and red spectra separately this allows us to compare a posteriori the detection rate, as well as redshifts and fluxes. This is described in the next sections, respectively referring to the two samples as 'Ultra-Deep blue' and 'Ultra-Deep red'. For each of the blue and red spectra the exposure time is 65000 seconds, allowing to reach a flux limit of $\sim 1.5 \times 10^{-18} \text{ erg/cm}^2/\text{s}$ (details below). The total sky area serendipitously covered is 3.3 arcmin^2 .

The noise of VIMOS spectra varies as a function of wavelength, as a result of a combination of different effects. First, the combination of the efficiency of VIMOS optics and the CCD quantum efficiency depends on the wavelength of the incident light. Second, the OH airglow sky emission lines are in a suite of bands which are dominating the background for $\lambda > 7500 \text{ \AA}$, and are not easy to subtract from the combined object+sky spectra in low to medium resolution spectra. As a result, spectra are noisier at the wavelengths of the OH bands. An added uncertainty on the flux level is also sometimes present at the position of serendipitous Ly α emission because the background subtraction performed by the VIMOS data processing pipeline VIPGI (Scodreggio et al., 2005) is optimized using the a-priori knowledge of the position of the VVDS primary target. As the serendipitous target is offset from the main target, the low order polynomial fit used to remove the background is made using some background points including the emission line, therefore artificially lowering the line flux. Third, the thin E2V detectors on VIMOS produce fringing which strongly affects the part of the spectra at $\lambda > 8000 \text{ \AA}$. As the VVDS has been using a low resolution $R \sim 230$ to maximize the number of objects in the survey, this produces a blend of the OH sky emission features,

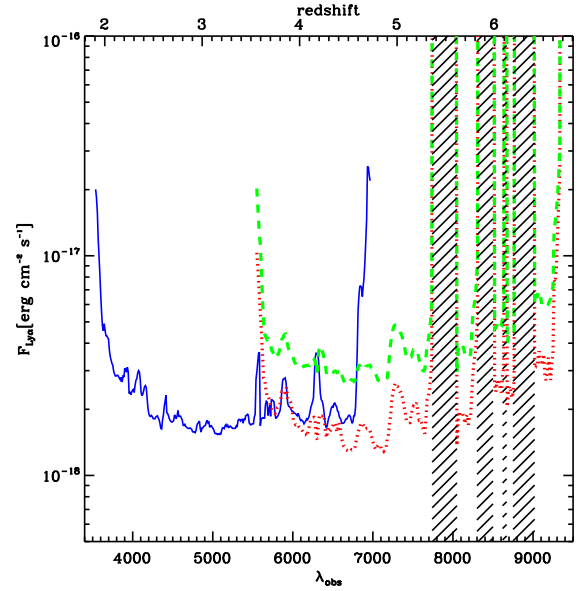


Fig. 1. Detection limits for the Ly α line, as a function of wavelength and redshift, for the three subsamples: Deep (green dashed line), Ultra-Deep red (red dotted line) and Ultra-Deep blue (blue line). The shaded regions indicate part of the spectra dominated by bright OH sky lines, where the rms of the background becomes too high to enable a secure line detection.

globally increasing the background noise at the position of the OH bands. As a result of these effects, the flux limit varies as a function of wavelength, hence of redshift. We determined the theoretical flux limit, separately for 'Ultra-Deep blue', 'Ultra-Deep red' and Deep, by measuring the typical rms at different wavelengths in the $2 - d$ spectra. Empirically, we decided to set the limit to 3σ in at least 5 contiguous pixels. The limits for the three subsamples are shown as a function of wavelength in Figure 1. It can be noted that the background, even for each of the three subset, is changing as a function of the wavelength and redshift. As a result of the bright OH skylines at $\lambda > 7500 \text{ \AA}$, a large part of the redshift range at $z > 5.5$ is in practice inaccessible. However, there are at least two very clean windows around $z=5.7$ and $z=6.5$, with a very low background corresponding to the absence of OH emission. The faintest flux limits can be observed in the range $4200 < \lambda < 7600 \text{ \AA}$, reaching down to very faint flux levels of $\sim 1.5 \times 10^{-18} \text{ erg/cm}^2/\text{s}$ at 3σ . The combination of sky area covered, wavelength range, and depth is unprecedented.

2.2. Photometry

The VVDS 0216-04 field benefits from extensive deep photometry. The field was first observed with the CFH12K camera in BVR I bands (Le Fèvre et al., 2004; McCracken et al., 2003), in the U band (Radovich et al. 2004) and K band (Iovino et al. 2005). More recent and significantly deeper observations have been obtained as part of the CFHT Legacy Survey in $ugri$ and z' (Goranova et al. 2009; Coupon et al. 2009), and as part of the WIRDS survey in J , H and K bands. The CFHTLS observations reach 5σ point source limiting magnitudes in i band of $i_{AB} \simeq 28$ while the WIRDS observations reach a 3σ point source limit of $K_{SAB} \simeq 23.5$ (McCracken et al., in preparation).

3. The Ly α sample

3.1. Serendipitous emission lines identification

The final database consists of ~ 1200 2-d spectra observed with both red and blue grism (Ultra-Deep dataset), and ~ 8000 2-d spectra observed with the red grism. For each of the 92 quadrants observed, the reduction code (VIPGI, Scodreggio et al. 2005) produces a frame in which the ~ 100 2-d spectra are arranged one above the other, with the spectral direction along the x-axis. With the purpose of identifying serendipitous lines, we built a data processing procedure that automatically masked out all the continua and the bad features (bright residuals and OH skylines). The unmasked area is then used to search for emission lines, and to compute the effective area covered by each slit on the sky. An object falling serendipitously in a slit will produce a spectrum with a combination of continuum and emission lines. For faint objects with strong lines, the continuum is not detected, and we are left with emission lines with a line profile as produced by the spectrograph. For point source objects, VIMOS produces a line profile along the slit (in the spatial direction) which is almost identical to the seeing profile (FWHM $\sim 1''$ or about 5 pixels). This is the projected equivalent slit size resulting from the object size convolved with the seeing profile and the slit profile on the spectral dispersion direction for a maximum of about 5 pixels corresponding to the 1 arcsecond slit width projection (or about 30\AA spectrally). The 2D line profiles produced are thus similar to point source images. For compact objects smaller than the atmospheric seeing disc, and if the seeing is smaller than the 1 arcsec slit width, the observed line profile in the spectral dimension will be dominated by the projected seeing profile. For extended objects the line profile becomes wider in the spatial direction leading to oval shaped emission lines. As these spectroscopic line images are similar to those of stars or galaxies on deep images, we blindly run SExtractor on the masked 2D spectra to automatically find all emission lines. This was followed by a visual inspection by two authors (PC and OLF) of all the objects detected by SExtractor, each producing a catalog of candidates. A further inspection has been conducted in order to find possible lines missed by SExtractor: we noted that lines too close to a bright continuum were not found by SExtractor, probably because of deblending problems. These two independent lists were then jointly examined by these two authors to decide if a candidate was to be kept, with more than 85% of the lists being unambiguously and independently selected by both authors. A fiducial catalog of *bona-fide* emission lines has then been built from this comparison. A more careful determination of the incompleteness and contamination will be presented in the next sections. In particular, the completeness is assessed using simulations in Section 3.4, and an estimate of the contamination is given in Section 3.2.

We obtain a total sample of 133 serendipitous emission line emitters, 105 found in the Ultra-Deep survey and 28 in the Deep. Most of these galaxies have no evident continuum appearing in the spectra. We show a random pick of 8 serendipitous lines in Figure 2 and 3.1. For each line, we show both the 2-d and 1-d spectra.

3.2. Ly α identification

Once the fiducial emission line catalog is built, we have to unambiguously assign a rest-frame wavelength to any given emission line. If one emission line is identified in a contiguous spectrum covering 3600 to 9350 \AA , there are several possibilities for the

line identification assuming a star-forming galaxy spectrum: below 3727 \AA the line is most probably Ly α , above 3727 \AA the emission line can be Ly α , [OII]3727 \AA , H β , [OIII]5007 \AA (assuming [OIII]4959 \AA is not detected, [OIII]5007/[OIII]4959 ≈ 3), or H α . In the spectrum of normal star forming galaxies, [OII], H β and [OIII] are most often present. Therefore, as a first approach we assumed that the emission lines could be [OII] at 3727 \AA , H β at 4861 \AA , [OIII] at 5007 \AA or H α at 6563 \AA , and we checked for other expected emission lines at different wavelengths in our spectral window. Using the typical line ratios for star-forming galaxies of average metallicity we estimate the flux of the other expected lines, and check whether they could be detected above our flux limit. However, the line flux ratios strongly depend on the galaxy metallicity. For example, typical ranges of line ratios are: [OIII]/[OII] = 0.1 \div 5, H α /[OII] = 0.3 \div 5 and H β /H α = 0.1 \div 0.8 (Lamareille et al. 2006; Maier et al. 2006; Tresse et al. 2007; Cowie&Barger 2008, Kewley&Ellison 2008). So, we decided to use the following line ratios, typical of galaxies with average metallicity: [OIII]/[OII] ~ 0.35 , H α /[OII] ~ 1 and H β /H α ~ 0.35 . Cases of extreme metallicity are discussed below.

Narrow-line type-II AGN with classical line ratios would be straightforward to identify given the broad wavelength range of our spectra. If we were to assign the single emissions lines to lines like CIV-1549, CIII-1909, or MgII-2800 we would expect to see other emission lines in our observed range either towards the UV (Ly α , CIV, CIII) or towards the red (MgII, [OII], [NeIII]). Broad line type-I AGN are also relatively easy to identify at our spectral resolution. We have not found any type-I or type-II AGN in our data, consistent with expected AGN counts in the area sampled (e.g. Bongiorno et al., 2007; Lamareille et al., 2009).

As the spectral window spans from 3600 \AA to 9350 \AA for the Ultra-Deep subsample and from 5500 \AA to 9350 \AA for the deep subsample, we analyze these samples separately.

- Ultra-Deep: 2 single lines in the Ultra-Deep are at $\lambda < 3727\text{\AA}$, and then can likely be identified as Ly α , while 103 are at $\lambda > 3727\text{\AA}$. Among the latter, 93 lines are at $\lambda < 6920\text{\AA}$. If they were [OII], we would to have [OIII] and H β in our spectral window. We estimate, using the line ratios reported above, that 75 of these 93 lines should be accompanied by either detectable [OIII] or detectable H β or both, but as they are not detected they are therefore most probably to be identified with Ly α . For the 10 emission lines at $\lambda > 6920\text{\AA}$, this argument cannot be used, because the possible [OIII] and H α emission would lie out from our spectral window. Using similar arguments, we can infer that none of the Ultra-Deep lines are H β , [OIII] or H α , because they would be always accompanied by at least one other line in our spectral window with a flux brighter than the flux limit.
- Deep: The deep subsample contains 28 serendipitous lines. Again, all of them can be in principle interpreted as both Ly α or [OII]. Since for the Deep the spectral window is smaller than for the Ultra-Deep, the same argument as for the ultra-deep tells us that only 7 of these lines are not [OII]. For the other 21, either a possible [OIII] emission is outside the spectral range, or it would be too faint to be detected. However, we can conclude also that the bulk of them are not H α , [OIII] or H β , because at least one other detectable line would be detected in our spectra.

From this first analysis, we can conclude that basically none of the serendipitous lines in the sample are H α , H β or [OIII],

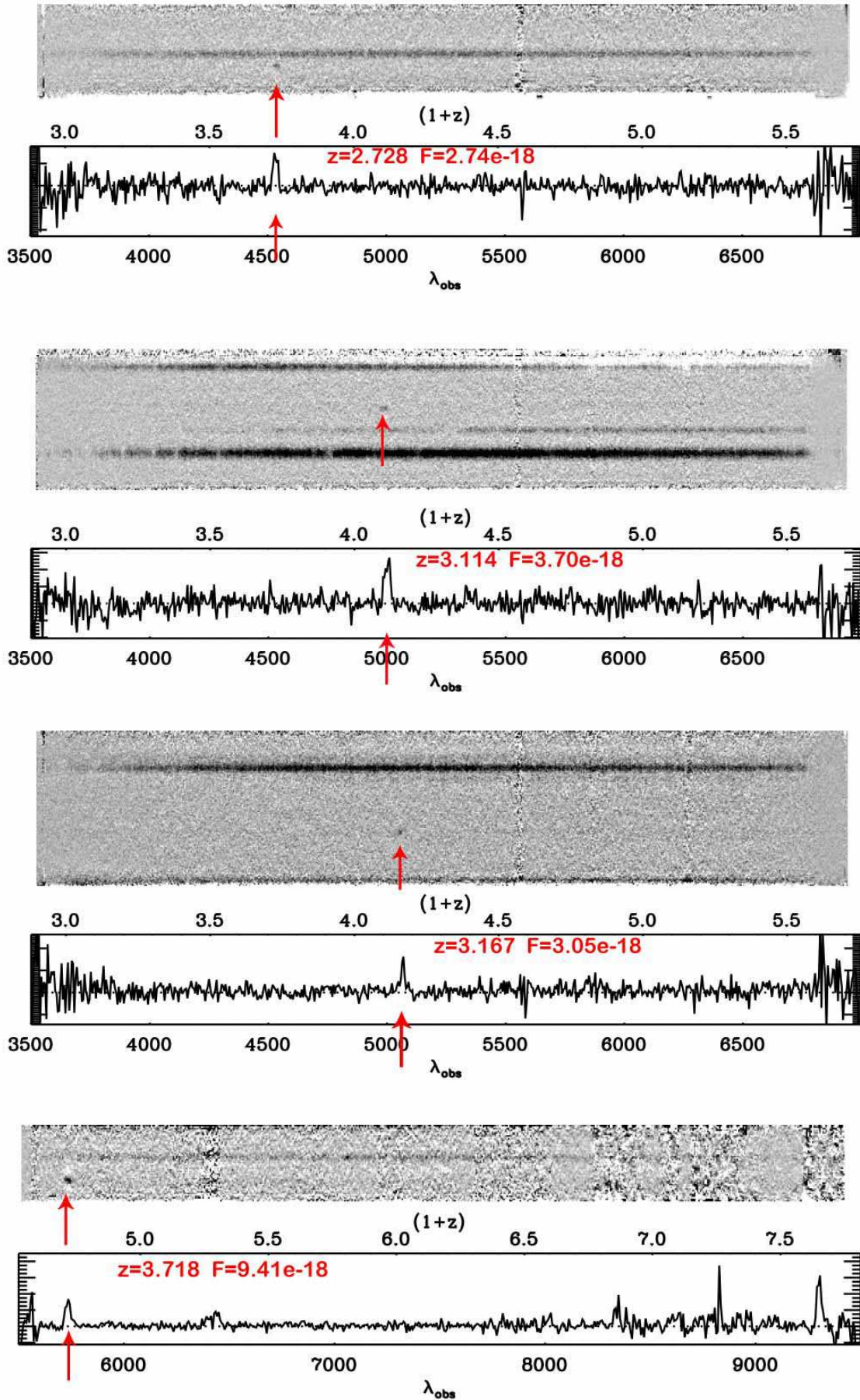


Fig. 2. Random selection of LAE candidates from the Ultra-deep blue dataset, ordered by increasing redshift. For each of them we show the full 2-d (top) and 1-d (bottom) spectra. The position of Ly α is indicated by an arrow on both the 2-d and 1-d spectra, and by a label reporting the redshift on the 1-d spectrum. The observed wavelength scale at the bottom of the 1-d spectrum is transformed into the redshift of Ly α at each wavelength on the top.

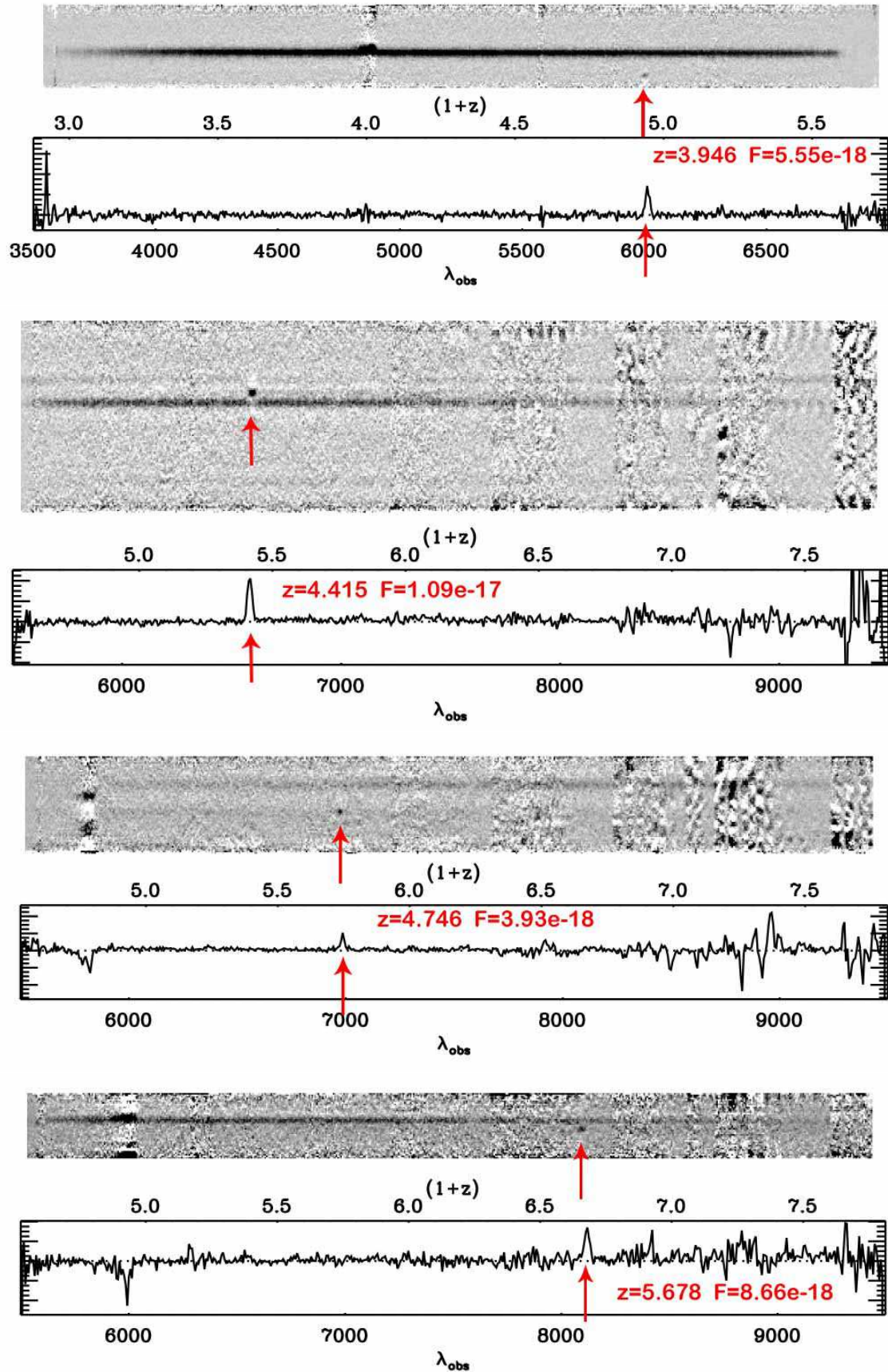


Fig. 3. Same as figure 2, for objects detected in the Ultra-deep red and in the Deep datasets.

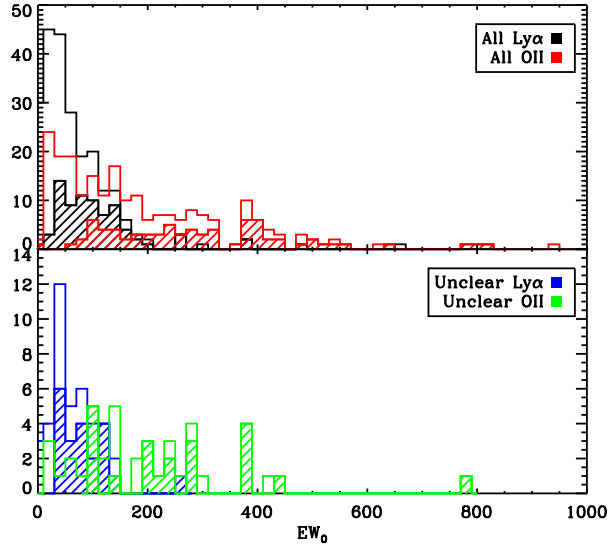


Fig. 4. *top panel:* For the full sample, the distribution of rest-frame EW if the lines are identified as Ly α (black histogram) or as [OII]3727 (red histogram). The filled histograms show objects without a detected continuum, for which the EW is a lower limit. *lower panel:* the same as the top panel, but for the 49 lines identified as ambiguous. The blue and green histograms represent respectively the rest-frame EW if the lines are identified as Ly α or as [OII]3727.

that 84 among the 133 *bona fide* serendipitous lines are not [OII], and that most of the line identification uncertainty for the other 49 emission lines is between [OII] and Ly α . We note that these findings will not change too much if we had used much lower values for the metallicity. Assuming, for example, [OIII]/[OII] \sim 10, if the serendipitous line was assigned to [OII], we should always have detected [OIII] for all lines with $\lambda < 6920$.

We can perform a further check in order to evaluate the contribution of Ly α and [OII] emission to the observed population. In particular, we measured the observed equivalent width of the lines to produce the distribution of the rest-frame EW for each of the two cases, as presented in Figure 4, for all the 217 lines as well as for the 49 ambiguous lines. While the distribution of the rest-frame EW for the lines if they are Ly α is mostly below 150 \AA , we find that if the lines were assigned to [OII], \sim 70% of the distribution would be with EW[OII] $>$ 100 \AA . Among the 49 galaxies that cannot be unambiguously classified as either Ly α or [OII], 37 would have EW[OII] $>$ 100 \AA . We compare this distribution to the distribution of EW[OII] observed for galaxies with $M_B \approx -18$ in the VVDS-Deep (Vergani et al. 2008) in the same redshift range $0.86 < z < 1.5$, and we note that 90% of the normal galaxy population has EW[OII] $<$ 100 \AA . At $z \approx 1$, galaxies with EW[OII] $>$ 100 \AA have only rarely been observed in deep spectroscopy surveys, and none with EW $>$ 150 \AA (Hammer et al., 1997; Vergani et al., 2008). Since we expect to have just 5 lines with EW[OII] $>$ 100 \AA (10% of 49), we can conclude that for about 32 (37-5) the identification is very likely to be Ly α . So, at the most we can identify the line as [OII] for 17 galaxies (49-32). We therefore conclude that

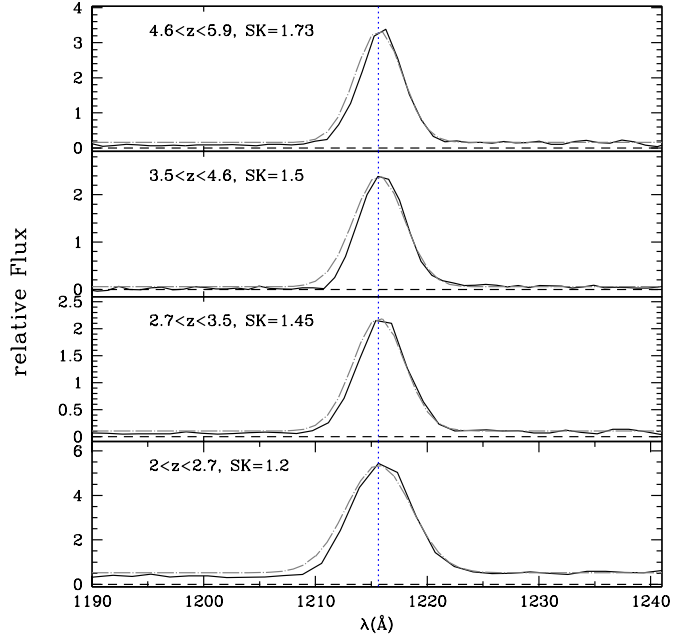


Fig. 5. Combined spectra for all serendipitous LAE in 4 redshift domains, centered on Ly α . The asymmetry of the line profile is clearly seen in each redshift range when comparing to a gaussian fit of the red wing of the line (long-dashed line). For each combined spectrum we report also the skewness calculated in the range $1201 < \lambda < 1231\text{\AA}$.

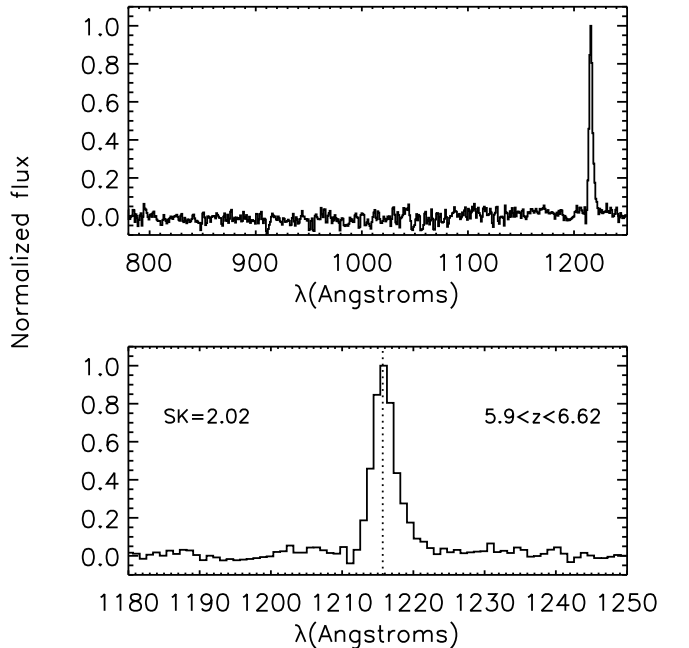


Fig. 6. Combined spectra for $5.9 < z < 6.62$. The top panel shows the continuum bluewards of the Ly α line. The bottom one focuses on the line, showing the asymmetric profile. The value for the skewness of the line is also reported.

about 10% of the single emission lines could be assigned to either [OII] or Ly α , while more 90% of them are most likely Ly α . Another check on the line identification with Ly α is to look at the line profile. Ly α line profiles are most often asymmetric, with a truncation towards the blue because of absorption by the

intergalactic medium, and an extended red wing because of complex velocity fields (Shapley et al., 2003; Ouchi et al., 2008). On individual objects, the line detection is not always of sufficient S/N to detect a line asymmetry, instead we produced the average normalized Ly α line profiles for LAE in different redshift ranges up to $z \sim 6$, as shown in Figure 5 (the description of the combination technique and a more detailed analysis of the combined spectra are presented in Section 4.3). The asymmetry of the profile is clearly seen at all redshifts, even in the lower redshift bins. For each combined spectrum we measured also the skewness of the line in the range $1201 < \lambda < 1231\text{\AA}$, that measures the degree of asymmetry of a given distribution. If the line profile would be perfectly described by a gaussian, that is by definition symmetric, the skewness would be zero. On the other hand, a positive value for the skewness indicates a distribution skewed towards red wavelengths. As Figure 5 shows, in each redshift bin between $2 < z < 5.9$ the skewness is positive and is increasing with redshift as expected from IGM absorption, reinforcing the primary identification with Ly α .

There are 6 galaxies with a single emission line in the atmospheric windows $8450 < \lambda < 8620$ and $9000 < \lambda < 9300$ clean of OH sky emission lines, and they observed equivalent widths $540 < EW < 1250\text{\AA}$. If these lines were [OII]3727 or H α , the rest EW would be $220 < EW < 510$ or $400 < EW < 880\text{\AA}$ with a mean EW=315 or 550 \AA respectively, clearly outside the range of EW for [OII] or H α emitting galaxies at $z \sim 1$. No sign of the broad component of an AGN which could produce high H α EW has been observed. We also produced the line profile of the 6 galaxies in this redshift range, reported in Figure 6. The resulting profile is clearly asymmetric, as confirmed by the positive value for the skewness. As other single emission line candidates with strong observed EW are even more unlikely than [OII]3727 or H α and should show other emission lines in our observed wavelength domain, we argue that the most likely possibility is that these emission lines are Ly α with $5.96 < z < 6.62$, making them some of the most distant galaxies found to date.

In summary, among the 133 emission lines identified serendipitously in the 2D spectra, we conclude that 124 are most likely Ly α , while a low fraction of 14 (10%) can be either Ly α or [OII]. In the following, we assume that all galaxies with ambiguous line assignment are Ly α .

3.3. Final sample

We completed the LAE sample by adding the primary VVDS spectroscopic targets that unambiguously have Ly α in emission. We found 70 Ly α emitters among the ~ 1200 Ultra-Deep primary targets, all at redshift $z < 3.5$, and 14 among the ~ 8000 Deep targets. The Deep survey is actually limited to $\lambda > 5500\text{\AA}$, hence it could not see Ly α at $z < 3.5$. All these galaxies have a high quality flag (larger than or equal to 2; Le Fèvre et al., 2010, in prep.) for the redshift, since they have other spectral features that allow to unambiguously identify the redshift and therefore classify them as Ly α emitters. They show in fact OI at 1303\AA , CII at 1333\AA , SiIV at 1397\AA , CIV at 1549\AA , and sometimes CIII at 1909\AA . The final sample is therefore made of 217 LAE, including 133 serendipitous LAE, and 84 LAE from the primary VVDS targets. The sample is summarized in Table 1.

For each emission line, we carefully measured the position of the line (and thus the redshift), the total flux in the line and the continuum. The continuum, in units of F_λ , is measured as close as possible to the red wing of the Ly α line, by averaging the counts between 1230 and 1250 \AA . From these fundamental

	U-DEEP blue	U-DEEP red	DEEP	total
Serend.	94 ¹ (46)	24 ¹ (7)	28(13)	133(66)
Targets	70	0	14	84

Table 1. The final sample of Ly α emitters, divided into serendipitous objects and spectroscopic targets. The number in parenthesis for the serendipitous galaxies indicates the objects with optical counterpart. Note:¹ 13 lines have been observed in both U-DEEP blue and U-DEEP red

quantities, the observed and rest-frame equivalent widths and the luminosities are derived:

$$L = 4\pi F d_l(z)^2 \quad EW_{rest} = F/C \frac{1}{1+z} \quad (1)$$

where L and F are respectively the luminosity and the flux in the line, z is the redshift of the line, $d_l(z)$ is the luminosity distance at the redshift of the line, EW_{rest} is the rest-frame Equivalent Width and C is the continuum around the line. Obviously, when the continuum is not detected, the derived equivalent widths are just a lower limit, and we used 1 sigma of the background as the continuum value.

Moreover, each luminosity can be converted to a star formation rate (SFR) combining the classical prescription to derive the SFR from H α Luminosity by Kennicutt (1998) and the expected ratio between Ly α and H α flux. In particular:

$$SFR(M_\odot yr^{-1}) = L_{H\alpha}(ergs s^{-1}) / (1.26 \times 10^{41}), \quad (2)$$

with H α flux corrected for internal extinction and valid for a Salpeter IMF. The conversion between H α and Ly α luminosity has been theoretically derived by Brocklehurst 1971 (assuming case B recombination):

$$L_{Ly\alpha} = 8.7 L_{H\alpha}, \quad (3)$$

and it does not account for dust and escape fraction corrections.

Combining the two gives:

$$SFR(M_\odot yr^{-1}) = L_{Ly\alpha}(ergs s^{-1}) / (1.1 \times 10^{42}). \quad (4)$$

In Figure 7 we report the flux and the position (both wavelength and redshift if the lines are identified as Ly α) for the three surveys separately. It can be noted that the Ultra-Deep blue is providing the biggest sample with 164 emission lines galaxies (94 serendipitous lines and 70 targets of the spectroscopy), while the Ultra-Deep red and the Deep contribute with respectively 24 and 42 emission lines galaxies. Note also that in a few instances we measure line fluxes that are weaker than the nominal flux limit at that wavelength: this is because the background, at each wavelength, is measured as the average of the backgrounds in the different quadrants and pointings. For some pointings, the background is lower than the average, and thus fainter lines can be detected.

3.4. Completeness simulations

As we saw in Fig. 1, the background of our spectra has a complicated structure, as there are strong variations with wavelength. To perform a statistical analysis of the number density evolution of Ly α galaxies, it is important to carefully determine, for each wavelength (and thus for each redshift), what is our capability to recover a line with a given luminosity.

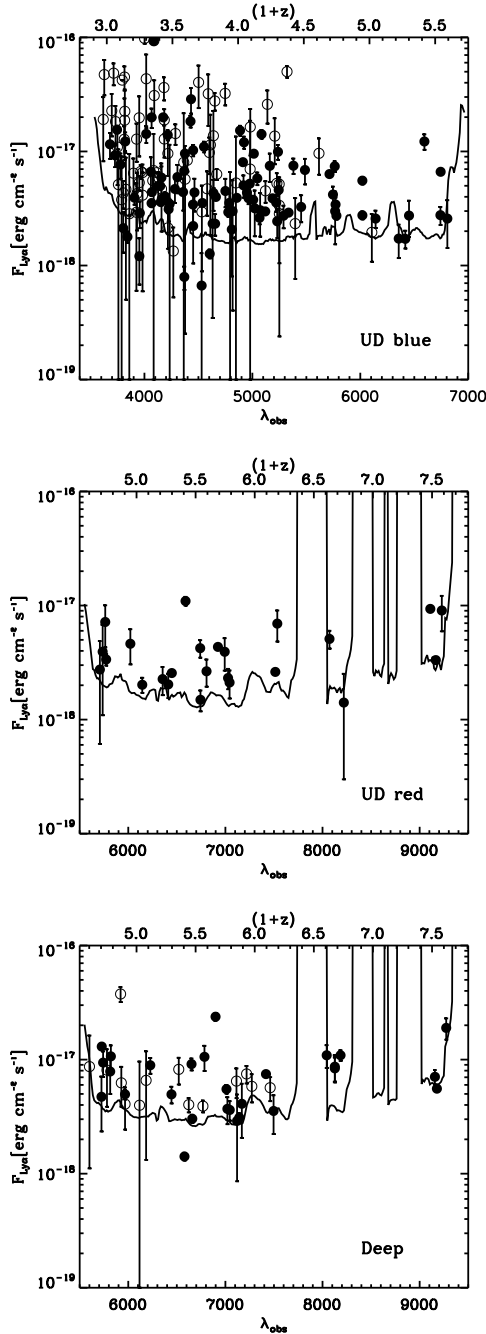


Fig. 7. For each sub-dataset, we show the flux versus redshift together with the flux limit as a function of the redshift and wavelength (*solid lines*). The flux limit is empirically measured on the 2-d spectra. Filled and open circles represent respectively serendipitous Ly α galaxies and targets with Ly α emission.

We performed a Monte Carlo simulation, building a catalog of 1000 fake lines for each dataset, for a total of 3000. Each line has a known flux, randomly extracted from a flat distribution between $F_{Ly\alpha} = 1 \times 10^{-18}$ and $F_{Ly\alpha} = 1 \times 10^{-16}$. The redshift is randomly extracted from a flat distribution between $z=2$ and $z=4.7$ (for blue spectra) and between $z=3.7$ and $z=6.7$ (for red spectra). The fake lines are then added at the wavelength corresponding to the known redshift, in a randomly extracted slit. Since emission lines in our sample are not or barely resolved either in the spatial or in the spectral directions (see next sec-

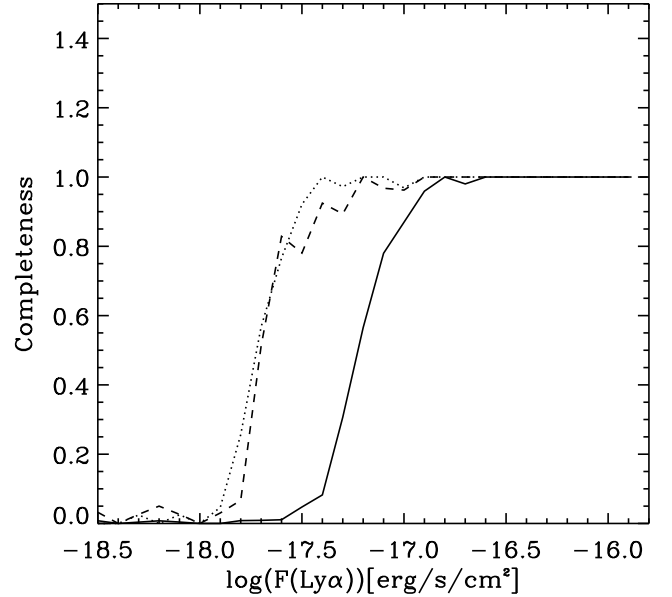


Fig. 8. Completeness in line identification from Monte Carlo simulation as a function of the flux, for the three subsamples: Deep (*solid line*), Ultra-Deep red (*dotted line*) and Ultra-Deep blue (*dashed line*).

tions), we chose to use simple gaussian profiles with FWHM of $1'' \times 30\text{\AA}$.

We attempted to recover these simulated lines, without a-priori knowledge of redshifts and fluxes, by applying the same procedure used on the real 2-d spectra, described in Section 3.1. The results are reported in Figure 8 presenting the completeness as a function of the line luminosity and of the redshift, for the three subsamples. We can see that Ultra-Deep blue & red and Deep are 50% complete respectively at $F_{Ly\alpha} \sim 2 \times 10^{-18}$ and $\sim 8 \times 10^{-18}$.

3.5. Slit flux loss

Since the slits used have sizes comparable to the seeing of the images, part of the line flux cannot be recovered and will be always lost. The flux loss depends on the offset between the galaxy and the slit center positions, on the size of the galaxy with respect to the slit width and on the atmospheric seeing. For an object perfectly centered in the slit, the flux loss will be minimal, but not zero. If the position of the object in the slit is known, as in the case of the objects with an optical counterpart, it is relatively easy to compute the flux loss. However, a significant number of galaxies in our sample do not have an optical counterpart within $\pm 0.5''$ from the expected position of the object along the slit and within $\pm 2''$ off axis in the direction perpendicular to the slit (see Section 4.2).

As we do not know for these galaxies their positions inside the slits, we cannot compute object by object the actual flux loss. This problem is common to all surveys of serendipitous Ly α emitters (e.g. Rauch et al. 2008; Lemaux et al. 2009), and is usually solved with a statistical approach for the objects with no detected counterpart. In this Section, we derive the slit flux loss as a function of the position of the object in the slit, so that we can correct the line flux for those objects with an optical counterpart, and then we estimate a statistical correction for the objects without any optical counterpart.

We start from the consideration that the bulk of our Ly α galaxies are unresolved in the spatial direction (see Section 4.2),

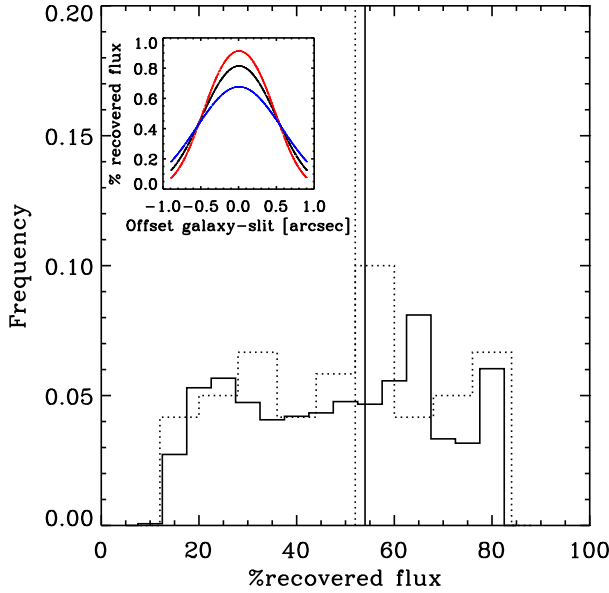


Fig. 9. Histogram of the percentage of recovered flux, for a set of a 3000 simulated lines randomly offset with respect to the center of the slit (solid line) and for the serendipitous lines (dotted line). The vertical lines show the median for the two distributions, around 55% of the recovered flux. The small inset shows the recovered flux as a function of the offsets for the simulated lines, for the 0.7, 0.9 and 1.2 arcsec FWHM lines (respectively in red, black and blue).

having sizes comparable with the seeing of the observations. The FWHM distribution in the spatial direction of the lines in our sample spans from 0.5 to 1.2 arcseconds, with 90% of them having $\text{FWHM}=0.7\div 1.2$ arcsec (see Figure 11). This implies that we can model them as gaussians, with fixed FWHM. We built a simulation in which an emission line object with a given FWHM is placed in a 1 arcsec slit at different positions with respect to the center of the slit until it is completely outside of the slit width. The small inset in Figure 9 shows the fraction of recovered flux as a function of the offset between the objects and the slit, for three seeing conditions $\text{FWHM}=0.7, 0.9$ and 1.2 arcsec (corresponding to $\sigma \sim 0.3, 0.38$ and 0.5 arcsec). If the galaxy was perfectly centered in the slit, only $\sim 70, 80$ and 90% of the flux would be recovered, respectively for the $1.2, 0.9$ and 0.7 arcsec FWHM lines; on the other hand, if the galaxy would be placed at $2\sigma=0.8$ arcsec outside the slit, only 20% of the light would be retrieved.

Thus, we can estimate that the slit flux loss for the 84 primary spectroscopic targets, that are perfectly centered in the slits, is around 15%, with a typical range between 10% and 30% depending on the seeing. For the serendipitous object with an optical counterpart, whose offset with respect to the center of the slit is known, we estimated the flux loss assuming they are compact under the average seeing conditions of a pointing. We show their distribution of the recovered flux in Figure 9.

In order to check if the percentage of recovered flux that we find for the serendipitous sample is reasonable, we use a Monte Carlo simulation. In particular, we generate 3000 2-dimensional gaussian profiles with FWHM randomly extracted between 0.7 and 1 arcsec, applying an offset between the position of the peak and the center of the slit randomly extracted between ± 1 arcsec. The distribution of the recovered flux for the 3000 lines is shown in figure 9. We note that the choice of $\pm 1''$ as maximum offset introduces an artificial cut-off at $\sim 10\%$ of the recovered

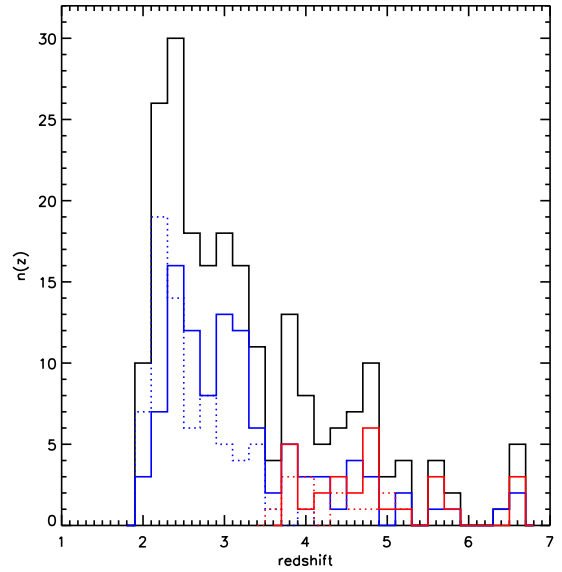


Fig. 10. Redshift distribution for the whole sample (black line), as well as for the different subsamples: solid lines show serendipitous lines, while dotted ones indicate primary spectroscopic targets; blue and red lines show the Ultra-Deep and deep subsamples, respectively.

flux. This choice however is justified by the fact that an hypothetical object placed offslit by more than $\pm 1''$ should have a true Ly α flux $> 10\times$ stronger than the one measured in the slit spectroscopy, hence its optical counterpart should be visible in photometry. There is an overall agreement from the result of this simulation and the flux loss estimated for the serendipitous lines with optical counterpart. For $\sim 40\%$ of the cases, the recovered flux is higher than 70%. The median of both histograms is $\approx 55\%$: we will use this value to correct the measured fluxes for the serendipitous lines with no optical detection in our sample.

4. Sample properties

4.1. Redshift distribution

In Figure 10 we show the redshift distribution for our sample. The distribution extends from $z = 2$ to $z = 6.7$, with a median $\langle z \rangle = 3$. We have 5 detections at $z \sim 6.5$ and 9 at $z \sim 5.7$. The main VVDS targets with Ly α come mainly from the Ultra-Deep survey, and interestingly, they show a different redshift distribution: even though the peak for the two subsample is around $z = 2.2 \div 2.5$, the serendipitous show a broader tail at $z > 4$, while 85% of the targets have $z < 4$. A simple Kolmogorov-Smirnov test rules out with more than 99% confidence that the two distribution are statistically equivalent. This reflects the different selection for the 2 subsamples: magnitude selected for the former, flux selected for the latter.

4.2. Optical counterparts and size distribution

We searched the deep CFHTLS ugriz images, including the combined ugriz stack, for optical counterparts of the 133 serendipitous LAE. In order to account for possible positional uncertainties, we required the counterpart to be within $\pm 0.5''$ from the position of the spectrum along the slit. Moreover, since even bright off-slit objects can show a detectable spectrum (see Sect. 3.5), we search for counterparts within $\pm 2''$ of axis. We found faint

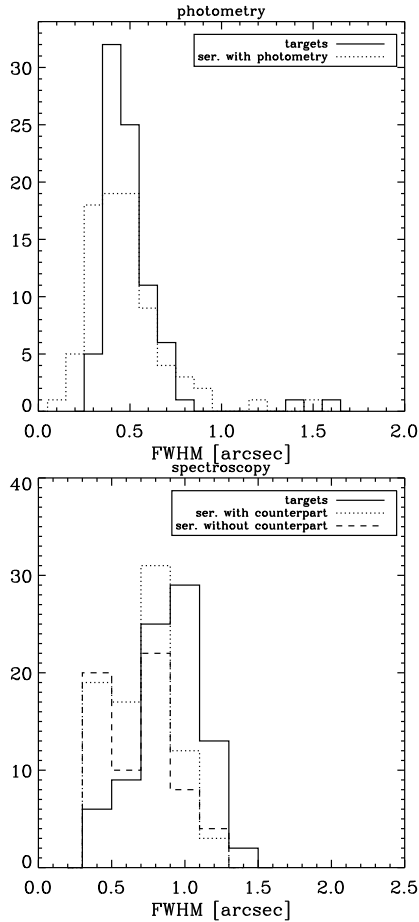


Fig. 11. Full width half maximum (FWHM) distribution as measured from the CFHTLS images (top panel) and from the Ly α 2-d spectra (bottom panel). Targets are shown with a solid line, serendipitous objects with and without photometric counterparts are shown with a dotted and dashed line, respectively. The CFHTLS image used has been built by stacking the 25% best-seeing exposures, and has a final PSF FWHM of about 0.5". In the top panel, we just show serendipitous objects with photometric counterpart.

counterparts for 53 (50%) and 13 (46%) LAE respectively in the ultra-deep and in the deep sample, with magnitudes i_{AB} ranging from 23.5 to 27.5. These counterparts are always $\pm 1''$ off axis at the most. For the remaining 67 objects we did not find an optical counterpart down to a magnitude $AB \sim 28$.

In Figure 11 we compare the Full Width at Half Maximum (FWHM) for the serendipitous Ly α emitters and the spectroscopic targets, as measured on the deep CFHTLS images and directly on the 2-d spectra of the Ly α line.

In particular, we used CFHTLS-D1 (VVDS-02h field) D-25 stack in the z -band, that has been built stacking the 25% best seeing images together resulting in a PSF FWHM of about 0.5 arcsec (see Table 26 of Goranova et al. 2009). Thanks to the better angular resolution, these images are very useful to check whether or not our galaxies are resolved in the spatial direction. On the other side, we are also interested in measuring the size for our sample also on the 2-d spectra, to check the assumption we made in Sect. 3.5, where we estimated the slit flux loss.

The FWHM of the serendipitous and main VVDS magnitude selected populations with optical counterparts measured in the D-25 stack are compared in the top panel of Figure 11. The distribution for both populations peaks at around 0.5 arcsec with a gaussian distribution width. This is expected from the measure-

ment errors on these faint objects if they are unresolved under the seeing of the D-25 stack. The width of the Ly α line measured on the 2-d spectra (bottom panel of Figure 11) indicates that the Ly α line is emitted from a compact region, as the size distribution is comparable to the seeing distribution of the spectroscopic observations. This is therefore indicating that most of the LAE are compact, both on the continuum and line emission.

From these measurements it is clear that the faint LAE population is compact in size. Interestingly, there is a clear lack of large objects (FWHM > 1–1.5 arcsec) in our sample. Faint LAE clearly have different sizes than the large Ly α blobs identified in the bright LAE population (Steidel et al. 2000; Matsuda et al. 2004; Ouchi et al., 2008). The weak continuum and Ly α sizes are in agreement with Venemans et al. (2005), Taniguchi et al. (2009), and the HST-based study of Bond et al. (2010). Our results support a picture where Ly α emission from faint LAE is compact and originates from the same area as the UV continuum as found by Bond et al. (2010), and we do not confirm the trend reported by Nilsson et al. (2009) of more extended sizes in the narrow band Ly α images than in the broad-band images. While extended Ly α emission like observed in Ly α blobs and Ly α halos is expected if Ly α is produced from resonant scattering on diffuse gas surrounding the galaxy, our data may indicate that the gas reservoir of faint LAEs is rather compact or that, if extended, it is only scattering a small fraction of the Ly α photons. We will explore the evolution with redshift of these properties in a forthcoming paper.

We show the size distribution measured directly on the 2-d spectra in the bottom panel of Fig. 11: due to the poorer seeing of these observations with respect to the CFHTLS ones, this distribution is peaked at 0.9 arcsec. Hence, this justifies our choice to simulate lines as gaussians with an average FWHM of 0.9 arcsec to estimate the slit flux loss in Section 3.5.

4.3. Spectral properties of the LAE

We produced combined spectra for all the Ly α in our sample, including primary VVDS targets as well as sources identified serendipitously. In order to preserve line shapes and to avoid averaging out faint features, we used accurate redshift measurements from a half-gaussian fit to the red wing of the Ly α lines, that has been used to determine the central wavelength of Ly α , hence the redshift. Each spectrum has then been de-redshifted to rest-frame, normalized using the continuum flux in 1400–1800Å up to $z=4.6$, 1400–1600Å for $4.6 \leq z \leq 5.9$, and the Ly α line itself for $5.9 < z \leq 6.7$, then averaged using a sigma-clipping algorithm. The results in several redshift ranges are shown in Figure 12 and Figure 13, for serendipitous and target objects, respectively. A number of spectral features can be readily identified at all z , including of course Ly α , but also prominent CIV in absorption as well as HeII in emission well detected in the two lowest redshift bins.

Bluer than Ly α we can see that the continuum is more absorbed as redshift increases, with a ratio ($f[1250 - 1350\text{Å}]/f[1100 - 1180\text{Å}]$) for serendipitous LAE of 1.34, 1.47, 2.0, 9.3 for redshifts $z \sim 2.3, 3, 4, 5.3$ respectively, and for target LAE a ratio of 1.41 and 1.51 for redshifts $z \sim 2.3, 3$ respectively. For our highest redshift objects $5.9 < z < 6.7$, uncertainties on the continuum blueward of Ly α only enables to state that this ratio is higher than 5. These measurements are comparable to the expected average extinction by the intergalactic medium, as Madau et al. (1995) predict ratios of 1.3, 1.5, 2.5 and 8.2 for

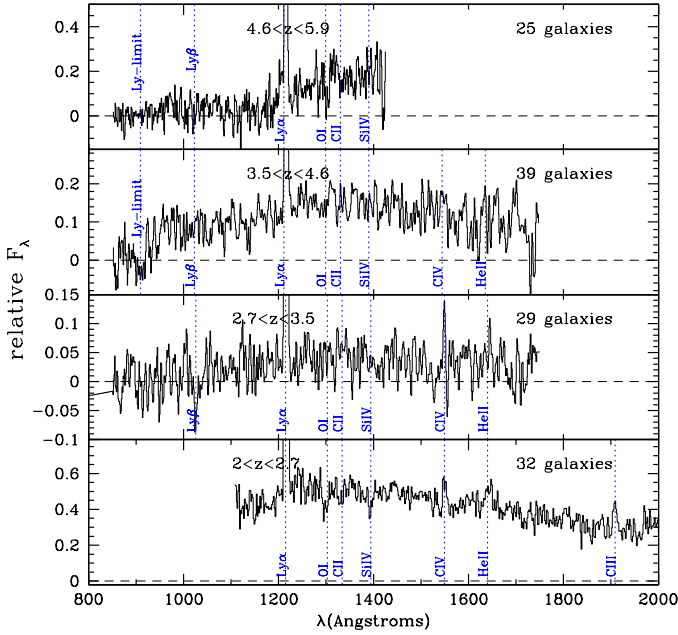


Fig. 12. Combined spectra of the serendipitous Ly α emitters, in several redshift ranges from $z=2$ to $z=5.9$. The displayed range of flux has been set to show faint continuum features, while the peak of the Ly α line is largely off-scale. Blue dotted lines indicate different spectral features depending on the redshift range: Ly-break at 912Å , Ly β at 1026Å , OI at 1303Å , CII at 1333Å , SiIV at 1397Å , CIV at 1549Å , HeII at 1640Å and CIII at 1909Å . The horizontal dashed lines indicate the level of zero flux.

$z \sim 2.3, 3, 4, 5.3$, respectively. This strengthens our identification of these emission line objects as LAE.

Ly β – 1026Å is readily observed, and the Lyman-break at 912Å is well detected for redshifts $z > 2.9$ placing this feature in our observed wavelength range, as expected.

To check for a difference between the targeted magnitude limited sample and the serendipitous LAE, we produced the combined spectra for all target LAE in the redshift domains $2 \leq z \leq 2.7$ and $2.7 < z \leq 3.5$ as shown in Figure 13, while above $z=3.5$ the serendipitous LAE dominate and their combined spectra are quasi identical to the spectra shown in Figure 12. Many spectral features are clearly detected in absorption: Ly β –1026Å , OI–1303Å , SiIV–1397Å . Besides Ly α , CIV–1549Å , HeII–1640Å and CIII–1909Å are all detected in emission.

The Ly α rest-EW increases from $38 \pm 1\text{Å}$ at $z \approx 2.3$ to 370 ± 150 at $z \approx 6.3$. This trend is probably the result of two effects: a general trend of increasing star formation at higher redshifts, and a difference between the observed galaxy populations, with less (more) luminous galaxies observed at lower (higher) redshifts. The mean EW of HeII–1640 for the full sample is $\text{EW}=1.4 \pm 0.2\text{Å}$, $2.0 \pm 0.1\text{Å}$ and $4.0 \pm 2.0\text{Å}$ at $z \approx 2.3$, $z \approx 3.1$, and $z \approx 4$ respectively, indicating the presence of a young stellar population a few 10^7 years old (Schaerer 2002). Considering only the serendipitous Ly α , the $\text{EW}(\text{HeII})$ is rising from 3.9 ± 0.4 at $z \approx 2.3$ to 14.5 ± 1.5 at $z \approx 3.1$. This is clearly indicating that a younger stellar population is present at the higher redshift. The difference of EW between the full Ly α sample and the serendipitous Ly α at $z \approx 3.1$ is significant, 4.0 ± 2.0 versus 14.5 ± 1.5 , possibly again a consequence of the

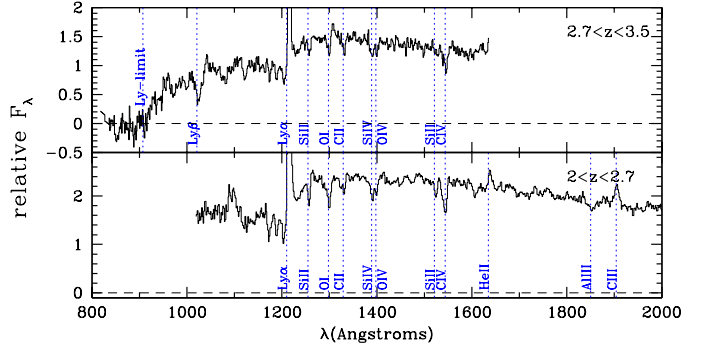


Fig. 13. Combined spectra of the target Ly α emitters in the redshift ranges $2 \leq z \leq 2.7$ and $2.7 \leq z \leq 3.5$. The displayed range of flux has been set to show faint continuum features, while the peak of the Ly α line is largely off-scale. The horizontal dashed lines indicate the level of zero flux.

different populations observed, Ly α in the serendipitous sample corresponding to fainter objects with stronger star formation or less extinction of the Ly α emitted photons. This difference at the same redshift could therefore indicate that continuum–faint Ly α contain younger stellar populations than continuum–bright Ly α . This will be the subject of further studies.

The Ly α line in the combined spectra has an asymmetric profile with the blue wing truncated and an extended red wing, as shown in Figure 5. This is expected as gas outflow and intergalactic absorption impose a sharp blue cutoff and a broad red wing. This Ly α shape and the clear detection of other expected emission and absorption features in the combined spectra provides further supporting evidence that the bulk of the lines in our sample are Ly α rather than [OII].

4.4. Properties of the 6 galaxies with $5.96 \leq z \leq 6.62$

The combined spectrum of the 6 galaxies identified with $5.96 < z < 6.62$ is shown in Figure 6. The continuum below Ly α is barely detected in this redshift range, consistent with a strong absorption by the intergalactic medium, while we detect a continuum at the 2σ level above 1215Å. The line profile shown in Figure 6 is also asymmetric in this redshift range, reinforcing the identification of the emission lines with Ly α .

The distribution of rest EW(Ly α) is in the range $70 < \text{EW} < 500$, with a mean $\text{EW}=310\text{Å}$ and a dispersion of 150Å . Malhotra&Rhoads 2002 suggested that $\text{EW}>300\text{Å}$ may indicate a top heavy IMF. However, our measurements are just around this limit, and moreover very uncertain, so we cannot draw any conclusions on this issue. Moreover, using Eq. 4 to convert luminosities to SFR for these 6 galaxies we obtain SFR in the range $4 < \text{SFR} < 22M_{\odot}\text{yr}^{-1}$, values that are not so extreme as to require a top-heavy IMF.

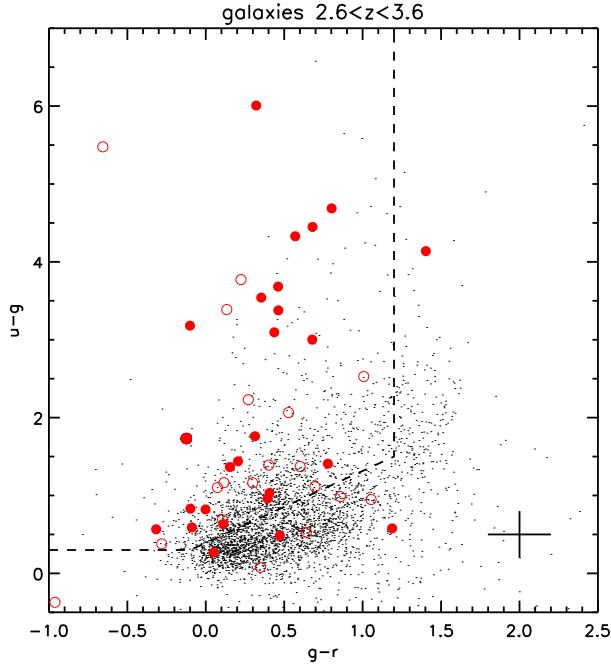


Fig. 14. UGR color-color plot for galaxies in our sample between $2.6 < z < 3.6$. Filled and open circles represent respectively targets and serendipitous objects with optical counterpart. Black points show galaxies at all redshifts. The dashed box indicates the drop-out region in which galaxies at such redshifts are expected to lie. The cross in the bottom right part of the diagram shows the typical error bars.

None of these galaxies are photometrically detected, neither in the single bands reaching as faint as $i_{AB} = 28$ (1σ), nor in the combined ugriz image, reaching an equivalent magnitude of $AB \approx 29$.

4.5. Photometric properties

In Figures 14 and 15 we show the ugr and gri diagrams for all galaxies in our sample (serendipitous and targets) at $2.6 < z < 4.2$. In fact, young star forming galaxies usually display very red colors around the 912Å Lyman limit: the flux below 912Å is virtually set to zero by the IGM absorption, while the star formation activity produces strong emission beyond Ly α line, producing a very pronounced and high S/N feature. This peculiarity is extensively used to look for high redshift ($z > 2$) galaxies (e.g. Steidel et al. 1999; Giavalisco 2002; Bouwens et al. 2007; 2009; 2010). We determined the part of the color-color plots in which high- z “dropouts” are expected to be convolving synthetic spectral energy distributions for star-forming galaxies with the SDSS photometric system filters.

In Fig. 14, about 80% of the galaxies with $2.6 < z < 3.6$ fall in the expected u-band dropout region. Similarly, in Figure 15, about 50% of the galaxies at $3.6 < z < 4.2$ fall in the expected g-band dropout region. The fact that a significant fraction of objects with secure spectroscopic redshifts falls out of the predicted color selection boxes has already been noted by Le Fèvre et al. (2005b), also for LAE as Gronwall et al. (2007) find a significant fraction of their sample outside of a UVR LBG box, and is mainly the result of the photometric measurement process (Le Fèvre et al., 2010, in prep.).

In Figure 16 we plot, for the objects with a photometric counterpart (primary targets and serendipitous), the equiv-

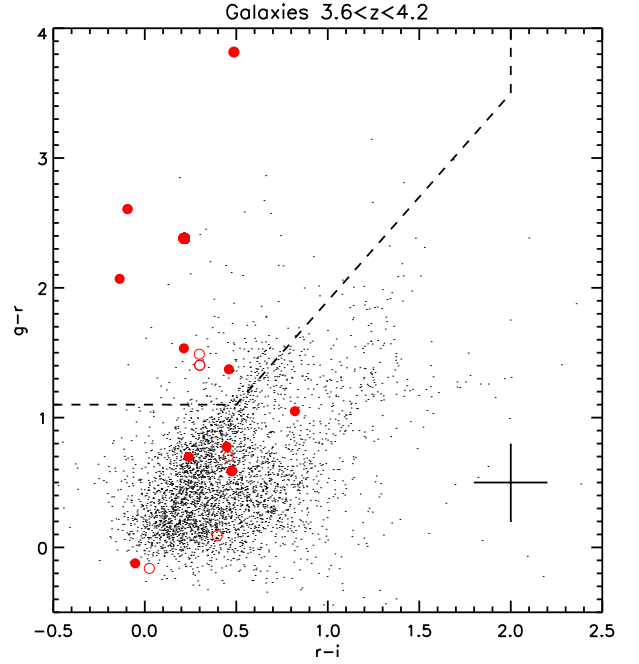


Fig. 15. GRI color-color plot for galaxies in our sample between $3.6 < z < 4.2$. Filled and open circles represent respectively targets and serendipitous objects with optical counterpart. Black points show galaxies at all redshifts. The dashed box indicates the drop-out region in which galaxies at such redshifts are expected to lie. The cross in the bottom right part of the diagram shows the typical error bars.

alent width of the Ly α lines as a function of the absolute magnitude in the UV at $\lambda_{rest}=1600\text{\AA}$, for three different redshift bins. Shimasaku et al. (2006), Ando et al. (2006) and Ouchi et al. (2008) suggested that objects with $M_{UV} < -21.5$ show typically low equivalent width ($EW < 20$), while objects with $M_{UV} > -21.5$ span a wide range of EW ($50 < EW < 150$). Our data are consistent with these findings, even though some of our galaxies with $M_{UV} < -21.5$ have just a lower limit to the EW. We note also that many of the serendipitous galaxies do not appear in this Figure, as they have no photometric counterparts.

In Figure 17 we compare the Ly α Luminosity, the Ly α Equivalent Width and the star formation rate inferred from the Ly α Luminosity for galaxies in our sample with others in literature. The aim of this figure is to show the different selection criteria for the various samples of Ly α emitters. Narrow band surveys typically select objects with $EW_0 > 20$ and do not reach Ly α emitters less luminous than $L_{Ly\alpha} = 10^{41.5}$, while our sample has no limits on the equivalent width and goes 0.5–1 dex deeper in luminosity. Overall, all the samples seem to follow a broad relation between Ly α luminosity and Ly α equivalent width. Moreover, it is clear that the typical object in our sample has a star formation rate $SFR \sim 1 M_{\odot} yr^{-1}$, with many having even smaller rates, while other samples have typically $SFR > 1 M_{\odot} yr^{-1}$, as expected from our deeper flux limit.

5. Luminosity functions

5.1. Formalism

We aim to combine the serendipitous and target Ly α emitters in the U-DEEP and DEEP surveys to produce luminosity functions at different redshifts. Since the targets and serendipitous objects have very different selection criteria, for the luminosity function

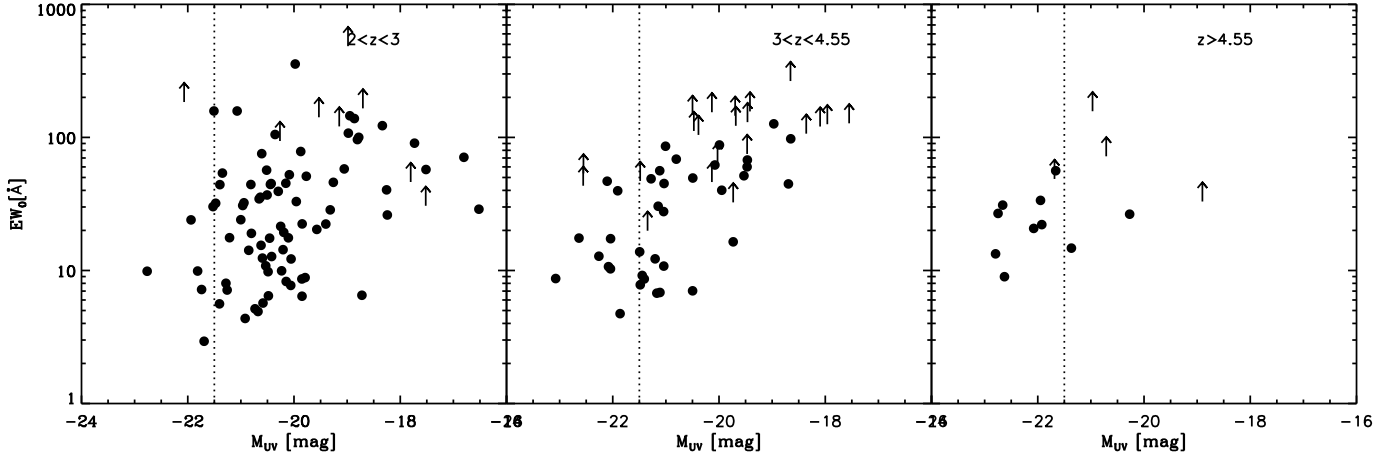


Fig. 16. Equivalent Width of the Ly α line as a function of the absolute magnitude at 1600Å, for the objects with photometric counterpart, in three different redshift bins. Objects with detected continuum are shown as filled dots. Objects without a detected continuum, for which the equivalent width is only a lower limit, are shown as upward arrows. The dotted line shows $M_{UV} = -21.5$: objects brighter than this limit show a deficit of large equivalent widths ($EW_0 > 20$).

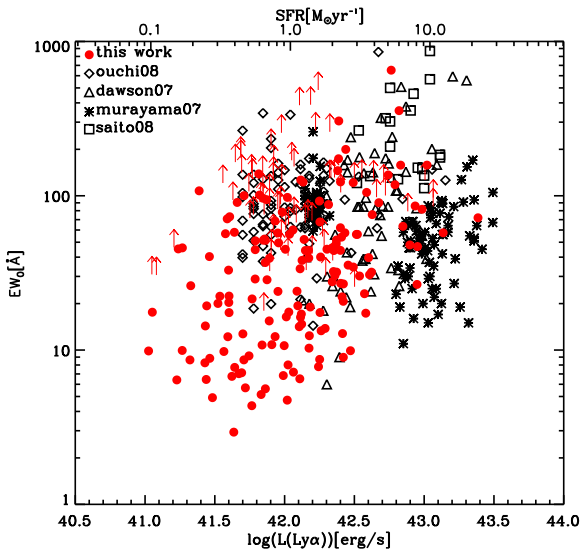


Fig. 17. Luminosity versus equivalent width for the galaxies in our sample (red points); filled and open circles indicate respectively galaxies with and without a detected continuum. For the latter, the measure of the EW is just a lower limit. Black diamonds, triangles, crosses and squares show respectively the samples of Ouchi et al. (2008), Dawson et al. (2007), Murayama et al. (2007) and Saito et al. (2008).

calculation we treated them independently. So, each galaxy from the target sample has a weight calculated with respect to the photometric selection, and each galaxy from the serendipitous sample has a weight calculated with respect to the spectroscopic selection.

Each of the two sample, however, is the combination of subsamples having different magnitude or Ly α flux limits and covering different areas: serendipitous LAE have been identified because their line flux exceeds the spectroscopic flux limit; those coming from the Ultra-Deep have a flux limit $\sim 1.5 \times 10^{-18} \text{ erg/cm}^2/\text{s}$, while those coming from the Deep survey have a flux limit of $\sim 5 \times 10^{-18} \text{ erg/cm}^2/\text{s}$. The VVDS primary spec-

troscopic targets are selected according to their magnitude in the I -band; those coming from the Ultra-Deep are selected to have $m_I < 24.75$, and those coming from the Deep to have $m_I < 24$.

To combine together subsamples reaching different flux (or magnitude) limits in different areas, we used the extended version of the $1/V_{max}$ formalism developed by Avni&Bahcall (1980). For each object we computed two effective volumes $V_{max}(j)$, one for the ultradeep limit and the other for the deep one (if the object is a target, the limit is the magnitude limit, if the object is a serendipitous one, the limit is the Ly α flux limit). So, for an object with redshift z assigned to the redshift bin $z_1 < z < z_2$:

$$V_{max}(j) = \theta(j) \int_{z_1}^{z_{sup}(j)} \frac{dV}{dz} dz \quad (5)$$

where z_{sup} is the minimum between z_2 and the redshift at which the object could have been observed within the limits of the j th selection, θ is the solid angle covered by the j th survey, and dV/dz is the comoving volume element. For each object, V_{max} is defined as:

$$V_{max} = \sum_j V_{max}(j). \quad (6)$$

This basically means that the brightest objects, that are visible in both the ultradeep and deep surveys, are weighted according to the effective volume accessible to them in both surveys, while the faintest one, that are visible just in the ultradeep survey are weighted just with respect to this latter. The target sampling rate and the success rate have been taken into account in computing the volumes for the targets. They are ~ 0.1 and ~ 0.3 for Ultradeep and Deep surveys, respectively.

The Ly α luminosities have been here corrected for the flux slit loss, as explained in Sect. 3.5: for the targets, the expected slit loss is 15%, and for the serendipitous sample is $\sim 45\%$. We verified that the choice of an average value for such correction do not affect our main results: in particular, the Schechter best-fit values presented in Section 5.2 do not change, within the errors, if the slit flux loss correction are randomly extracted for each object from the distribution shown in Fig. 9. Finally, we combined

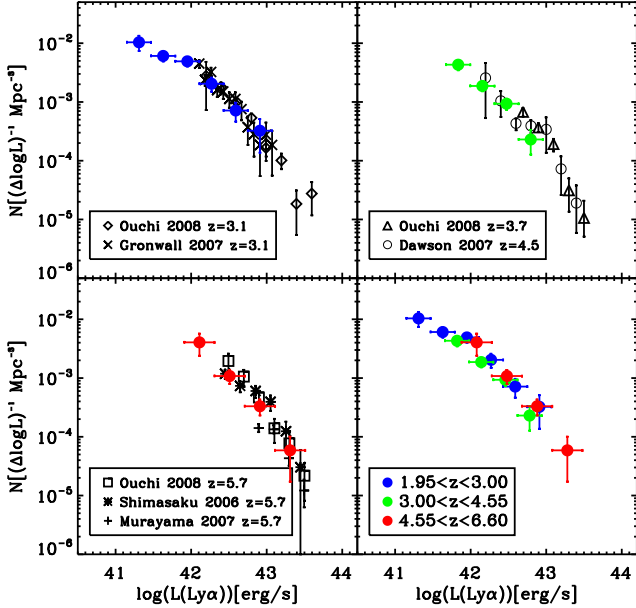


Fig. 18. LAE Luminosity function in different redshift bins. No IGM absorption correction has been applied here. Upper left, upper right and bottom left panels indicate $2 < z < 3.2$, $3.2 < z < 4.55$ and $4.55 < z < 6.6$ respectively. The error bars reflect the poissonian errors. Black datapoints show literature data, spanning from $z=3$ to $z=5.7$: diamonds, triangles and squares represent Ouchi et al. (2008) at respectively $z = 3.1$, $z = 3.7$ and $z = 5.7$; asterisks, plus signs, crosses and circles indicate respectively Shimasaku et al. (2006) at $z = 5.7$, Murayama et al.(2007) at $z = 5.7$, Gronwall et al. (2007) at $z = 3.1$ and Dawson et al. (2007) at $z = 4.5$. We group together our measurements in the different redshift bins in the bottom right panel, to show that within the error bars, the Ly α LF does not evolve from $z = 2.5$ to $z = 6$.

the two V_{max} for them using Equation 6. Moreover, a completeness correction has been applied to each object according to its flux and redshift, both for targets and for serendipitous emitters.

Once we have V_{max} for both the targets and serendipitous objects, we compute the galaxy number density for each $\Delta \log(L)$ and Δz bin as:

$$\phi(L, z) = \frac{1}{\Delta \log(L)} \sum_n \frac{1}{V_{max}} \quad (7)$$

where n is the number of objects in that bin.

5.2. Evolution of the luminosity functions

We estimated the luminosity functions for 3 redshift bins: $z = 1.95 - 3.$, $z = 3. - 4.55$, $z = 4.55 - 6.6$ in order to keep enough galaxies per redshift bin for a reliable estimate of the LF. The results are shown in Figure 18.

When comparing our datapoints in these different redshift intervals, we can see that the observed apparent luminosity function (i.e. the non-IGM corrected LF) does not evolve in the redshift range $z \simeq 2.5$ to $z \simeq 6$ within our error bars. Although our data cover a slightly wider redshift interval they are in agreement with the literature data, within the error bars. This is quantified below.

The unprecedented depth of our survey enables to extend the luminosity function at $z = 2 - 3$. down to $\log(L_{Ly\alpha})=41.3$, about

one order of magnitude deeper than literature data at similar redshifts. This allows us to strongly constrain the slope of the luminosity function at $z \sim 2.5$. This parameter is extremely important, because a small change of this slope can produce a large change in the luminosity density.

We assumed here that the luminosity function of Ly α emitters is well represented by a Schechter law (Schechter 1976):

$$\Phi(L)dL = \Phi^*(L/L^)^\alpha \exp(-L/L^*)d(L/L^*) \quad (8)$$

We obtained the best-fit functions for the 3 redshift bins using this Schechter function. As a first try, we fitted the luminosity functions in the 3 redshift intervals allowing all the 3 parameters describing the Schechter function to vary. However, by doing this, the typical luminosity L^* in the first two bins and the slope α in the high redshift bin are poorly constrained. Indeed, in the first two bins we do not have Ly α galaxies brighter than $10^{43} \text{ erg/cm}^2/\text{s}$, and in the last one we do not observe emission lines fainter than $10^{42} \text{ erg/cm}^2/\text{s}$. So, we decided to use other datapoints in the literature to constrain L^* in the first two bins. In particular, we averaged the L^* values obtained by Ouchi et al. (2008) and Gronwall et al. (2007) at $z = 3.1$, obtaining $\log(L^*) = 42.7$. So, in our fit procedure we fixed $\log(L_{Ly-\alpha}) = 42.7$ in the first two bins. We verified that this approach is equivalent to including Ouchi et al. (2008) and Gronwall et al. (2007) datapoints with $\log(L_{Ly\alpha}) \gtrsim 43$ to ours and performing the fit. Moreover, we constrained α in the last bin to the average of the value in the first two bins. The best-fit parameters are reported in Table 5.2.

Importantly, we note that the luminosity functions reported above are not corrected for absorption by the intergalactic medium. The Ly α flux from high- z sources is generally absorbed by neutral hydrogen present in the IGM, that absorbs the blue wing of the Ly α line, producing an asymmetric line profile (Hu et al. 2004; Shimasaku et al. 2006). We therefore measure IGM absorbed Ly α fluxes, and not *intrinsic* Ly α fluxes. Moreover, the amount of absorption is not the same at different redshifts: at high z the amount of intervening intergalactic medium is larger. As a consequence, if the *observed i.e. apparent* luminosity functions do not evolve from $z \sim 2.5$ to $z \sim 6$, the *intrinsic* one positively evolves. The IGM optical depths have been estimated in various studies (i.e. Madau 1995, Fan et al. 2006 and Meiksin 2006): all the authors agree that the amount of absorption increases from $\sim 15\%$ at $z \sim 3$ to $\sim 50\%$ at $z \sim 6$ (at this redshift, basically all the blue side of the line is absorbed). Using the standard radiative transfer prescription by Fan et al. (2006) for the IGM optical depths, we can obtain the intrinsic luminosities L_{int} from the observed L_{obs} . At $z \sim 2.5$, 4.2 and 6 the ratio L_{obs}/L_{int} is respectively 0.91, 0.73 and 0.52.

In Figure 19 we show instead the *intrinsic* luminosity functions, corrected for the IGM absorption according to the prescription of Fan et al. (2006), together with our Schechter fits to the data.

The first main result from this analysis is that there does not seem to be a strong evolution of the *apparent* luminosity function between $z \sim 6$ and $z \sim 2.5$, within our error bars. In fact, looking at Fig. 18 we see that within our 1σ errors, the luminosity functions in the different redshift bins overlap; moreover, looking at the Schechter best fit parameters in Table 5.2, we can see again that within 1σ the Schechter parameters do not evolve. On the other hand, by looking at the *intrinsic* luminosity functions in Fig. 19, we do see an evolution between $z \sim 6$ and $z \sim 4$, while no sizeable evolution is observed between $z \sim 4$ and $z \sim 2$. The observed evolution can be parametrized with the evolution

z	$z = 1.95 \div 3$	$z = 3 \div 4.55$	$z = 4.55 \div 6.6$
α	$-1.6^{+0.12}_{-0.12}$	$-1.78^{+0.10}_{-0.12}$	-1.69
Φ^*	$7.1^{+2.4}_{-1.8} \times 10^{-4}$	$4.8^{+0.8}_{-0.8} \times 10^{-4}$	$9.2^{+2.3}_{-1.9} \times 10^{-4}$
$\log(L_{uncorr}^*)$	42.70	42.70	$42.72^{+0.10}_{-0.12}$
$\log(L_{corr}^*)$	42.74	42.83	$43.0^{+0.10}_{-0.12}$

Table 2. Schechter Function Parameters. $\log(L_{uncorr}^*)$ and $\log(L_{corr}^*)$ indicate respectively the value uncorrected and corrected for the IGM absorption. Error bars give the 1σ confidence levels. Values have been fixed during the fitting procedure when no error bars are shown.

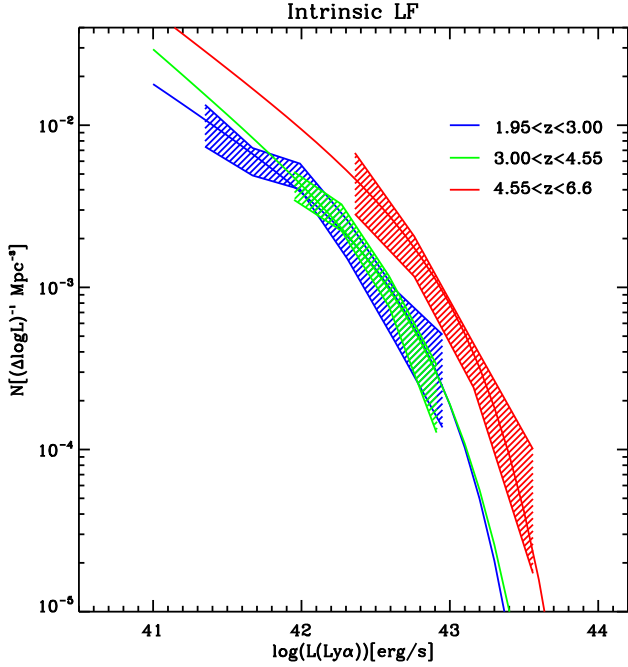


Fig. 19. We report here our estimates of the intrinsic luminosity functions, corrected for the IGM absorption (shaded regions). Blue, green and red indicate respectively $1.95 < z < 3$, $3 < z < 4.55$ and $4.55 < z < 6.6$ ranges. Solid lines show our best fits to the data.

in L^* , that is at $z \sim 6$ about 1.8 times higher than in the first bin. However, its significance level is only 1.5σ .

The second interesting result comes from our ability to constrain the faint end of the luminosity function. We find slopes $\alpha = -1.6^{+0.12}_{-0.12}$ at $z \sim 2.5$ and $-1.78^{+0.10}_{-0.12}$ at $z \sim 4$. Our data formally exclude a flat slope $\alpha \sim -1$ at 5 and 6.5σ , at these two redshifts. Our slope values are significantly better constrained than the best value of 1.36 and the marginalized value of $-1.49^{+0.45}_{-0.34}$ found at $z \sim 3.1$ by Gronwall et al. (2007), a consequence of the 10 times fainter flux limit of our sample. Note that other authors, who again do not have deep enough data, do not try to fit α , but they rather fix it to some plausible value (-1, -1.5 and -2 for Ouchi et al. 2008; -1.6 for Dawson et al. 2007; -1.2 and -1.6 for Lemaux et al. 2009). Our analysis therefore establishes the first reliable estimate of the faint end slope of the luminosity function of Ly α galaxies at $z < 5$.

It is also important to state that the possible “non-Ly α ” emitters in our sample, described in Sect. 3.2, do not strongly affect these results. First of all, the luminosity distribution of the “ambiguous” lines (the 49 lines that cannot be unambiguously identified as Ly α based on the line ratios) is similar to that of the global sample, and thus it is not expected to affect the slope determination. However, it is possible that in the $4.55 < z < 6.6$ redshift

bin the contamination is higher than in the others. In fact, for all the lines at $\lambda > 6920$ (corresponding to $z(\text{Ly}\alpha) \gtrsim 4.7$), we cannot check for other lines in the spectra, if the line is identified as [OII] (see Sect.3.2). However, we showed that the contamination is not expected to be higher than 10%, based on the EW distribution. Thus, assuming that all the 17 lines that can be identified as [OII] are at $z > 4.7$ would decrease the luminosity function in the last bin of a factor of 50% at the most. This would imply a weaker evolution of the luminosity function from $z = 6$ to $z = 4$.

5.3. Evolution of the star formation rate density

With these new constraints on the evolution of the Ly α luminosity function at these redshifts, it is interesting to estimate the contribution of the Ly α emitters to the global star formation rate density of the Universe. This is not trivial, as Ly α emission produced not only by star formation activity, but also by other processes like cooling radiation, AGN activity or shock winds. Moreover, Ly α emission is attenuated by IGM and dust.

We are computing here the SFRD using only the *intrinsic* Ly α luminosity functions. In order to estimate the contribution of the galaxies in our sample, we integrated the luminosity function from $L_{\text{Ly}\alpha} = 0.04 \times L^*$ to $\log(L_{\text{Ly}\alpha})=44$ (roughly the interval covered by our data). We then converted these Ly α luminosity densities in star formation rate densities by using Equation 4.

The derived star formation rates are shown in Figure 20, together with the most recent estimates of the SFRD at redshift between $z=0$ and $z=6$. Ouchi et al (2008) and Gronwall et al. (2007) use a sample of narrow band selected Ly α emitters, while the other estimates are based on the UV galaxy luminosity function.

We can see that our measurements show a slight evolution of the Ly α SFRD between $z \sim 2.5$ and $z \sim 4$, and a much more significant evolution from $z \sim 4$ and $z \sim 6$. Our values are compatible within the errors to those obtained by Ouchi et al. (2008).

When comparing our estimates of the Ly α SFRD with the UV-derived ones, we see that the total contribution of Ly α galaxies to the global star formation density at $z \sim 2 - 6$ is important, increasing from $\sim 20\%$ at $z \sim 2.5$ to $\sim 100\%$ at $z \sim 6$. This implies that the Ly α emission is a good tracer of the star formation, this statistically implies that, while at redshift $z \sim 2$ only a small fraction of the galaxies contributing to the star formation history of the universe also show a Ly α emission, all the galaxies at $z \sim 6$ do show Ly α in emission. In other words, the so called *escape fraction*, that is the fraction of Ly α emission produced by the star formation that actually escapes the star formation regions changes a lot with the cosmic epoch, from 20% at $z = 2.5$, reaching up to 100% at $z \sim 6$. This seems to indicate that the mechanism which is absorbing the Ly α photons in most of the galaxies at $z = 2$ is not effective at $z \sim 6$, as is expected in a very low dust medium. However, dust estimates at $z \simeq 5 - 6$ show that the dust content should be sufficient to produce significant Ly α photons absorption (e.g. Bouwens et al. 2009).

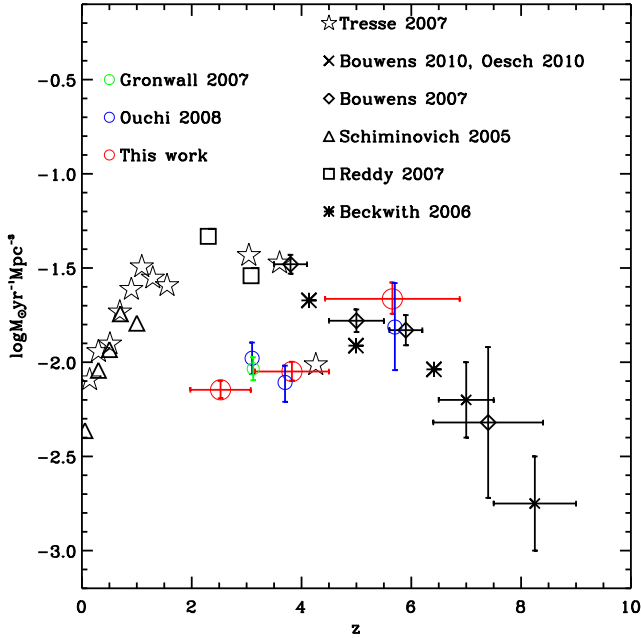


Fig. 20. Evolution of the star formation rate density as a function of the redshift, inferred integrating the intrinsic Ly α luminosity functions down to $0.04 \times L^*$. Red open circles are our data, while blue and green open circles represent other Ly α SFRD respectively by Ouchi et al. (2008) and Gronwall et al. (2007). , Open triangles, open squares, open lozenges, stars and crosses are UV estimates respectively by Schiminovich et al. (2005), Reddy et al. (2008), Bouwens et al. (2007), Beckwith et al. (2006), Tresse et al. (2007) and Bouwens et al. (2010)

Alternatively, it is possible that the UV luminosity function based on Lyman break galaxies searches is based on more and more incomplete counts at increasingly high redshifts, and that the current UV-derived SFRD are underestimates (e.g. Le Fèvre et al. 2005b; Paltani et al. 2007). Current estimates of the luminosity density at $z \simeq 5 - 6$ agree within a factor 2–3 or so (Bouwens et al., 2007, 2009), and will need new generation surveys to be improved.

6. Summary

In this paper we have reported the discovery of 217 faint LAE in the range $2 \leq z \leq 6.62$ from targeted and serendipitous very deep observations using the VIMOS multi-slit spectrograph on the VLT. Adding together the areas covered by each slitlet combined to the wide wavelength coverage 5500–9350Å of the Deep survey and 3600–9350Å for the UltraDeep, we surveyed effective sky areas of 22.2 arcmin^2 and 3.3 arcmin^2 respectively. This produces a survey volume of $\sim 2.5 \times 10^5 \text{ Mpc}^3$, observed to unprecedented depth $F \sim 1.5 \times 10^{-18} \text{ erg/s/cm}^2$. This volume is about one order of magnitude bigger than all other spectroscopic surveys produced up to now at comparable fluxes: van Breukelen, Jarvis & Venemans (2005) sampled 10^4 Mpc^3 down to $1.4 \times 10^{-17} \text{ erg/cm}^2/\text{s}$; Martin et al. (2008) sampled $4.5 \times 10^4 \text{ Mpc}^3$ down to similar fluxes in a narrow redshift range. Narrow band imaging surveys sampled bigger volumes than ours, but to a shallower flux: Ouchi et al. (2008) covered a volume of $\sim 10^6 \text{ Mpc}^3$, down to fluxes $\sim 2 \times 10^{-17} \text{ erg/cm}^2/\text{s}$. Serendipitous surveys have been presenting low number of objects (Sawicki et al., 2008), even if somewhat

deeper (Malhotra et al., 2005; Rauch et al., 2008). We are therefore sampling deeper into the LAE luminosity function as we discussed in section 5.2.

From an observational point of view, we demonstrate the efficiency of blind LAE searches with efficient multi-slit spectrographs. The success of our approach is the result of combining a broad wavelength coverage to a large effective sky area, with long integration times, made possible by the high multiplex of the VIMOS instrument. The broad wavelength coverage has been essential to secure the spectroscopic redshifts from one single observation, without the need for follow-up to confirm the Ly α nature of the emission lines detected. This observing efficiency compares favorably with the time needed to perform narrow band imaging searches followed by multi-slit spectroscopy, and comparing the wide range in redshift covered by the former versus a narrow range for the latter. When the density of faint LAE is high, of the order several LAE/arcmin², multi-slit spectrographs become more efficient to secure a large number of confirmed sources than narrow band imaging searches, while at bright fluxes covering a wide field is essential to find rarer sources and narrow band imaging is more efficient. The two approaches will therefore remain complementary.

Our main findings are the following:

1. We found a total of 217 LAE with confirmed spectroscopic redshifts in the range $2 \leq z \leq 6.62$, 133 coming from the serendipitous discovery in the multi-object spectrograph slits of the VVDS (105 from the Ultra-Deep and 28 from the Deep), and 84 coming from targeted VVDS observations of galaxies with $17.5 \leq i_{AB} \leq 24.75$ (Le Fèvre et al., 2010, in prep.). About 50% of the Ultra-Deep and 40% of the Deep serendipitous targets have a detected optical counterpart down to magnitude $AB \sim 28$ in deep CFHTLS images.
2. The observed projected density of LAE with a Ly α emission brighter than $F \sim 1.5 \times 10^{-18} \text{ erg/s/cm}^2$ in the range $2 \leq z \leq 6.6$ is 33 LAE per arcmin², with 25 LAE per arcmin² with $2 \leq z \leq 4.5$ and 8 LAE per arcmin² with $4.5 < z \leq 6.62$. The corresponding volume density of faint LAE with $L(\text{Ly}\alpha) \geq 10^{41} \text{ ergs.s}^{-1}$ is $\sim 4 \times 10^{-2} \text{ Mpc}^{-3}$, a high density not yet observed at these redshifts.
3. The mean rest-frame EW(Ly α) of LAE in our sample range from about 40Å at $z \sim 2 - 3$ to $\sim 300 - 400$ at $z \sim 5 - 6$, and the star formation rate covers a wide range $0.1 - 20 \text{ M}_\odot \text{ yr}^{-1}$, assuming no ISM or IGM extinction and a Salpeter IMF. The HeII-1640Å emission has EW $\sim 4 - 14$ at $z \sim 2 - 4$ indicating the presence of young stars of a few Myr. We therefore detected vigorously star forming galaxies as well as galaxies with star formation comparable to dwarf starburst galaxies at low redshifts.
4. The Ly α apparent luminosity function does not evolve between $z=2$ and $z=6$, within the error bars of our survey. Taking into account the average differential evolution in the IGM absorption with redshift therefore translates into a positive evolution of the intrinsic Ly α LF of about 0.5 magnitude from $z \sim 2 - 3$ to $z \sim 5 - 6$.
5. We obtain a robust estimate of the faint end slope of the LAE luminosity function from a large sample of spectroscopically confirmed LAE. It is very steep: we find $\alpha \simeq -1.6$ at $z \sim 2.5$ and 1.8 at $z \sim 4$.
6. The SFRD contributed by Ly α galaxies is increasing from $5 \simeq 10^{-3} \text{ M}_\odot \text{ yr}^{-1} \text{ Mpc}^{-1}$ at $z \simeq 2.5$ to $\simeq 2 \times 10^{-2} \text{ M}_\odot \text{ yr}^{-1} \text{ Mpc}^{-1}$ at $z \simeq 6$. The contribution of the Ly α galaxies to the total SFRD of the universe as inferred by UV luminosity functions reported in the literature increases from $\sim 20\%$ at $z=2.5$

to $\sim 100\%$ at $z=6$. This seems to imply that all the galaxies that are forming stars at $z = 6$ must show Ly α emission, therefore are in a very low dust medium. At $z=2.5$ 80% of the star forming galaxies must have the Ly α emission produced by star formation blocked by some mechanism so that only 20% of the star forming galaxies show Ly α emission. A direct consequence would be that the Ly α escape fraction varies from 0.2 at $z \simeq 2.5$ to about 1 at $z \simeq 6$. This result would remain robust only if the total SFRD estimates based on UV luminosity functions using Lyman break galaxies identifications are complete.

The new VVDS measurements reported here bring a new important constraint to the LAE LF with a steep faint end slope observed at $2 < z < 4.5$. This implies that LAE with star formation rates of a few $10^{-1} M_{\odot} \text{yr}^{-1}$ comparable to that of low redshift dwarf star forming galaxies are dominating the LAE SFRD at these redshifts. While it remains to be proven that the faint end slope of the LF stays steep going to still higher redshifts, assuming the slope $\alpha \simeq 1.7$ as implied by our measurements at $2 < z < 4.5$ would imply that the LAE population is becoming the dominant source of star formation producing ionizing photons in the early universe $z \sim 5-6$, becoming equivalent to that derived from Lyman Break Galaxies searches. The steep faint end slope further implies that during reionisation sub- L_{*} galaxies may have played an important role in keeping the universe ionized.

These results further demonstrate that efforts dedicated to constraining the evolution of the luminosity function of high redshift LAE will remain an important tool to probe into the reionisation period.

Acknowledgements. The authors acknowledge the anonymous referee for the constructive comments provided. PC acknowledges Sara Salimbeni for the useful discussions.

References

- Ando, M., Ohta, K., Iwata, I., et al., 2006, ApJ, 645, L9
 Avni, Y., and Bahcall, J. N., 1980, ApJ, 235, 694
 Beckwith, S. V. W., Stiavelli, M., Koekemoer, A. M., et al., 2006, AJ, 132, 1729
 Bond, N. A., Feldmeier, J. J., Matkovic, A., et al., 2010, ApJ, 716, 200
 Bongiorno, A., Zamorani, G., Gavignaud, I., et al., 2007, A&A, 472, 443
 Bouwens, R.J., Illingworth, G.D., Franx, M., and Ford, H., 2007, ApJ, 670, 928
 Bouwens, R.J., Illingworth, G. D., Franx, M., et al., 2009, ApJ, 705, 936
 Bouwens, R.J., Illingworth, G. D., Oesch, P. A., et al., 2010, ApJL, 709, 133
 Brocklehurst, M., 1971, MNRAS, 153, 471
 Coupon, J., Ilbert, O., Kilbinger, M. et al., 2009, A&A, 500, 981
 Cowie, L. L., & Hu, E. M., 1998, AJ, 115, 1319
 Cowie, L. L., & Barger, A. J., 2008, ApJ, 686, 72
 Cuby, J.G., Le Fèvre, O., McCracken, H., et al., 2003, A&A, 405, 19
 Dawson, S., Rhoads, J. E., Malhotra, S., et al., 2007, ApJ, 671, 1227
 Deharveng, J.-M., Small, T., Barlow, T. A., et al., 2008, ApJ, 680, 1072
 Djorgovski, S., Spinrad, H., McCarthy, P., and Strauss, M.A., 1985, ApJ, 299, L1
 Finkelstein, S. L., Rhoads, J. E., Malhotra, S., and Grogan, N., 2009, ApJ, 691, 465
 Fan, X., Strauss, M. A., Becker, R. H., et al., 2006, AJ, 132, 117
 Garilli, B., Le Fèvre, O., Guzzo, L., et al., 2008, A&A, 486, 683
 Gawiser, E., van Dokkum, P. G.; Gronwall, C., et al., 2006, ApJ, 642, 13
 Gawiser, E., Francke, H., Lai, K., et al., 2007, ApJ, 671, 278
 Giavalisco, M., Koratkar, A., Calzetti, D., 1996, ApJ, 466, 831
 Giavalisco, M., 2002, ARA&A, 40, 579
 Goranova, Y. Hudelot, P. Magnard, F., et al., 2009, The CFHTLS T0006 Release, http://terapix.iap.fr/cplt/table_synr0006.html
 Grove, L. F., Fynbo, J. P. U., Ledoux, C., et al., 2009, A&A, 497, 689
 Gronwall, C., Ciardullo, R., Hickey, T., et al., 2007, ApJ, 667, 79
 Guaita, L., Gawiser, E. Padilla, N., et al., 2010, ApJ, 714, 255
 Hammer, F., Flores, H., Lilly, S. J., et al., 1997, ApJ, 481, 49
 Hu, E. M., et al., 2004, AJ, 127, 563
 Iovino, A., McCracken, H. J., Garilli, B., et al., 2005, A&A, 442, 423
 Kashikawa, N., et al., 2006, ApJ, 648, 7
 Kennicutt, R. C., 1998, ApJ, 498, 541
 Kewley, L. J., & Ellison, S. L., 2008, ApJ, 681, 1183
 Kunth, D., Mas-Hesse, J. M., Terlevich, E., et al., 1998, A&A, 334, 11
 Lamareille, F., Contini, T., Brinchmann, J., et al., 2006, A&A, 448, 907
 Lamareille, F., Brinchmann, J., Contini, T., et al., 2009, A&A, 495, 53
 Lemaux, B. C., Lubin, L. M., Sawicki, M., et al., 2009, ApJ, 700, 20
 Le Fèvre, O., Saisse, M., Mancini, D., et al., 2003, SPIE, 4841, 1670
 Le Fèvre, O., Vettolani, G., Garilli, B., et al., 2005, A&A, 439, 845.
 Le Fèvre, O., Paltani, S., Arnouts, S., et al., 2005b, Nature, 437, 519
 Madau, P., 1995, ApJ, 441, 18
 Maier, C., J.; Carollo, C. M., Meisenheimer, K., et al., 2006, ApJ, 639, 858
 Malhotra, S., & Rhoads, J. E., 2002, ApJL, 565, 71
 Malhotra, S., Rhoads, J. E., Pirzkal, N., et al., 2005, ApJ, 626, 666
 Martin, C. L., Sawicki, M., Dressler, A. & McCarthy, P., 2008, ApJ, 679, 942
 Mas-Hesse, J. M., Kunth, D., Tenorio-Tagle, G., et al., 2003, ApJ, 598, 858
 Matsuda, Y., Yamada, T., Hayashino, T., et al., 2004, AJ, 128, 569
 Matsuda, Y., Yamada, T., Hayashino, T., et al., 2005, ApJL, 634, 125
 McCracken, H. J., Radovich, M., Bertin, E., et al., 2003, A&A, 410, 17
 Meiksin, A., 2006, MNRAS, 365, 807
 Murayama, T., Taniguchi, Y., Scoville, N. Z., et al., 2007, ApJS, 172, 523
 Nilsson, K. K., Moller, P., Moller, O., et al., 2007, A&A, 471, 71
 Nilsson, K. K., Tapken, C., Moller, P., et al., 2009, A&A, 498, 13
 Ouchi, M., Shimasaku, K., Furusawa, H., et al., 2003, ApJ, 582, 60
 Ouchi, M., Shimasaku, K., Akiyama, M., et al., 2008, ApJS, 176, 301
 Oesch, P. A., Bouwens, R. J., Illingworth, G. D., et al., 2010, ApJL, 709, 16
 Partridge, R. B., & Peebles, J. E., 1967, ApJ, 147, 868
 Paltani, S., Le Fèvre, O., Ilbert, O., et al., 2007 A&A, 463, 873
 Pentericci, L., Grazian, A., Fontana, A., et al., 2007, A&A, 471, 433
 Pirzkal, N., Malhotra, S., Rhoads, J. E., and Xu, C., 2007, ApJ, 667, 49
 Radovich, M., Arnaboldi, M., Ripepi, V., et al., 2004, A&A, 417, 51
 Rauch, M., Haehnelt, M., Bunker, A., et al., 2008, ApJ, 681, 856
 Reddy, N., Steidel, C. C., Pettini, M., et al., 2008, ApJS, 175, 48
 Rhoads, J. E., & Malhotra, S., 2001, ApJL, 563, 5
 Saito, T., Shimasaku, K., Okamura, S., et al., 2008, ApJS, 657, 1076
 Sawicki, M., Lemaux, B. C., Guhathakurta, P., et al., 2008, ApJ, 687, 884
 Schaefer, D., 2002, A&A, 382, 28
 Scodreggio, M., Franzetti, P., Garilli, B., et al., 2005, PASP, 117, 1284
 Shapley, A., Steidel, C. C., Pettini, M., and Adelberger, K. L., 2003, ApJ, 588, 65
 Schechter, P., 1976, ApJ, 203, 297
 Schiminovich, D., Ilbert, O., Arnouts, S., et al., 2005, ApJL, 619, 47
 Shimasaku, K., Kashikawa, N., Doi, M., et al., 2006, PASJ, 58, 313
 Steidel, C. C., Adelberger, K. L., Giavalisco, M., et al., 1999, ApJ, 519, 1
 Steidel, C. C., Adelberger, K. L., Shapley, A. E., et al., 2000, ApJ, 532, 170
 Taniguchi, Y., Murayama, T., Scoville, N. Z., et al., 2009, ApJ, 701, 915
 Tapken, C., Appenzeller, I., Gabasch, A., et al., 2006, A&A, 455, 145
 Tresse, L., Ilbert, O., Zucca, E., et al., 2007, A&A, 472, 403
 Vergani, D., Scodreggio, M., Pozzetti, L., et al., 2008, A&A, 487, 89
 van Breukelen, C., Jarvis, M. J., and Venemans, B. P., 2005, MNRAS, 373, 26
 Venemans, B. P., Rottgering, H. J. A., Miley, G. K., et al., 2005, A&A, 431, 793
 Yang, Y., Zabludoff, Ann I., Davé, R., et al., 2006, ApJ, 640, 539